J. Fluid Mech. (2007), *vol.* 581, *pp.* 287–321. © 2007 Cambridge University Press
doi:10.1017/S0022112007005642 Printed in the United Kingdom

Numerical study of a transitional synthetic jet in quiescent external flow

RUPESH B. KOTAPATI[1], RAJAT MITTAL[1]
AND LOUIS N. CATTAFESTA III[2]

[1]Department of Mechanical and Aerospace Engineering,
The George Washington University, Washington, DC 20052, USA

[2]Department of Mechanical and Aerospace Engineering,
University of Florida, Gainesville, FL 32611, USA

(Received 8 December 2005 and in revised form 21 December 2006)

The flow associated with a synthetic jet transitioning to turbulence in an otherwise quiescent external flow is examined using time-accurate three-dimensional numerical simulations. The incompressible Navier–Stokes solver uses a second-order accurate scheme for spatial discretization and a second-order semi-implicit fractional step method for time integration. The simulations are designed to model the experiments of C. S. Yao *et al.* (*Proc. NASA LaRC Workshop*, 2004) which have examined, in detail, the external evolution of a transitional synthetic jet in quiescent flow. Although the jet Reynolds and Stokes numbers in the simulations match with the experiment, a number of simplifications have been made in the synthetic jet actuator model adopted in the current simulations. These include a simpler representation of the cavity and slot geometry and diaphragm placement. Despite this, a reasonably good match with the experiments is obtained in the core of the jet and this indicates that for these jets, matching of these key non-dimensional parameters is sufficient to capture the critical features of the external jet flow. The computed results are analysed further to gain insight into the dynamics of the external as well as internal flow. The results indicate that near the jet exit plane, the flow field is dominated by the formation of counter-rotating spanwise vortex pairs that break down owing to the rapid growth of spanwise instabilities and transition to turbulence a short distance from the slot. Detailed analyses of the unsteady characteristics of the flow inside the jet cavity and slot provide insights that to date have not been available from experiments.

1. Introduction

Synthetic jets have emerged as versatile actuators with potential applications ranging from thrust vectoring of jets (Smith & Glezer 2002) to turbulence control in boundary layers (Rathnasingham & Breuer 1997, 2003; Lee & Goldstein 2001) and active control of flow separation (Wygnanski 1997; Smith *et al.* 1998; Amitay *et al.* 1999; Crook, Sadri & Wood 1999). The versatility of these actuators is primarily attributed to the following factors: (*a*) the forcing provided by synthetic jets is unsteady and this can be more effective than steady jets; (*b*) since the jets are synthesized from the working fluid, they eliminate the need for complex fluid circuits and accumulators; and (*c*) actuation frequency, amplitude or waveform can usually be tuned to a particular flow configuration.

A typical synthetic jet actuator consists of a jet orifice or slot opposed on one side by an otherwise sealed cavity and flush mounted on the other side to a fluid dynamic surface. Time-periodic changes in the volume of the cavity are brought about by some mechanism such as an oscillating piston or a piezoelectric diaphragm. These changes in volume of the cavity cause alternate expulsion and ingestion of the fluid across the slot with zero net mass flux (ZNMF). This process is often accompanied by the generation of a stream of vortices at the edges of the orifice/slot which impart finite momentum and vorticity into the surrounding fluid. Interaction of these vortical structures with the external flow field can trigger instabilities and enhance mixing in the external flow. When these synthetic jets operate in a boundary layer they can sometimes lead to the formation of closed recirculation regions in the mean flow (Smith & Glezer 1997; Amitay *et al.* 1997; Mittal, Rampunggoon & Udaykumar 2001) which modify the local as well as global characteristics of the flow.

A variety of experimental techniques have been used to investigate these ZNMF actuators. One of the earliest investigations of streaming motions was by Meissner (1926) who studied the attenuation of very high-frequency sound waves within a body of the fluid away from solid boundaries. Ingard & Labate (1950) studied the impedance of orifices by applying an orifice plate to a circular tube driven by sound waves and reported the effects of circulation caused by acoustic streaming. Andres & Ingard (1953) looked at the acoustic streaming at high Reynolds numbers caused by the attenuation of the transmitted sound waves near solid boundaries due to viscous effects. Mednikov & Novitskii (1975) used an oscillating piston and bellows mechanism in a resonant tube to produce zero-net mass-flux jets resulting from the dissipation of acoustic energy in the cavity. Lebedeva (1980) used the propagation of high-amplitude sound waves through a pipe mounted with an orifice plate to create a round jet and studied acoustic streaming in the vicinity of the orifices. Sheen, Lawrence & Raptis (1989) used cavitation-controlled ultrasonic agitators to create streaming motions in water.

James, Jacobs & Glezer (1996) synthesized a round turbulent water jet normal to a resonantly driven diaphragm flush mounted to a submerged flat plate. The jets were reported to result from time-periodic coalescence of vortex rings that are produced by secondary flow around cavitation bubbles formed at the centre of the diaphragm. Smith & Glezer (1998) synthesized a nominally two-dimensional jet by oscillatory motion of a flexible wall-mounted diaphragm in a shallow cavity. They investigated the near-field formation and evolution of jets using Schlieren images and hot-wire measurements of cross-stream distributions of the velocity components. They observed that the vortex pairs which are initially laminar after roll-up become unstable and that the cores of the vortex pairs break down into small-scale structures owing to rapid growth of instabilities. Yao *et al.* (2004*b*) (also see Yao *et al.* 2004*a*; Rumsey *et al.* 2004) presented velocity measurements of synthetic jets in quiescent air obtained using time-periodic oscillation of a wall-mounted piezo-electric diaphragm in an enclosed cavity. In this experiment, velocity measurements of the external flow were made using three different techniques, namely, hot-wire anemometry, laser-Doppler velocimetry (LDV) and particle image velocimetry (PIV).

A number of numerical simulations of synthetic jet flows have also been reported in the literature. Kral *et al.* (1997) reported two-dimensional incompressible calculations of both laminar and turbulent synthetic jets, the latter obtained by the solution of unsteady Reynolds-averaged Navier–Stokes (URANS) equations with Spalart–Allmaras (SA) one-equation turbulence closure. In these simulations, the flow within the cavity was not modelled and different analytic velocity profiles at the orifice exit were examined. Turbulent solutions showed good agreement with the mean velocity profiles measured by Smith & Glezer (1997). However, further away from the jet, vortices in the turbulent simulations were smeared by turbulent diffusion and the lack of three-dimensionality in the laminar predictions failed to capture the breakup of the vortex train observed in the experiments.

Rizzetta, Visbal & Stanek (1999) investigated two- and three-dimensional flow fields of finite aspect-ratio synthetic jets using direct numerical simulations (DNS) of unsteady compressible Navier–Stokes equations. Simultaneous solutions of the flow field in the external region, slot region and jet cavity were obtained using the chimera overset zonal mesh methodology on Cartesian grids. The motion of the diaphragm in the cavity was modelled by sinusoidally varying the position of the lower boundary. When internal cavity flow became periodic after several cycles, the velocity profile at the slot exit was recorded for one complete cycle and specified as a boundary condition at the slot exit in the subsequent cycles, thereby eliminating the need for modelling the cavity flow. The exterior flow field was then constructed using high-order compact-difference schemes in conjunction with non-dispersive spatial filters by enforcing symmetry conditions along the jet centreline that precluded asymmetric interactions between vortices across the centreline. Three-dimensionality in their simulations helped capture the breakdown of external flow into a turbulent jet, a phenomenon observed in the experiments, but missed in any strictly two-dimensional calculations. Mallinson, Hong & Reizes (1999) arrived at the same conclusion by comparing their experimental measurements with their URANS simulations of round jet, with κ–ϵ turbulence closure, performed along the same lines as Kral *et al.* (1997) by assuming an analytic velocity distribution at the slot exit, but using symmetry conditions along the jet centreline.

The first set of numerical simulations that included an accurate model of the jet cavity were carried out by Mittal *et al.* (2001). These two-dimensional simulations employed a Cartesian-grid-based immersed boundary method (Ye *et al.* 1999; Udaykumar *et al.* 2001) which allowed for the inclusion of complex-shaped moving boundaries. A realistic representation of the vibrating diaphragm was included in the simulations, and the synthetic jet flow was examined for both quiescent and grazing external flows. Simulations of jets in a crossflow boundary layer were used to examine the formation and scaling of closed mean recirculation zones downstream of the jet exit. Utturkar *et al.* (2003) carried out a detailed two-dimensional computational study using the same solver, and examined the sensitivity of the jet to the design of the jet cavity. Design changes examined in this study included changes in the cavity aspect-ratio as well as in the placement of the oscillating diaphragm. The general conclusion was that wide-ranging changes in the cavity design have a limited effect on the jet emanating from the cavity. Based on this, it was suggested that the jet flow may be computed/modelled with sufficient fidelity without precisely matching the cavity design. However, compressibility effects were not included in these simulations and it was noted that the conclusions regarding flow insensitivity to cavity design would potentially only be limited to the incompressible flow regime. This point is crucial for the current study and will be discussed in more detail in a later section.

One of the key features of synthetic jets in quiescent flow is the formation of vortex dipoles (rings) at the lips of the slot (orifice) which are expelled in a direction away from the jet exit. The numerical simulations of Mittal *et al.* (2001) indicated that depending on the operational parameters of the jet, these vortices could in fact either be expelled or ingested back into the cavity. Thus ‘jet formation’ seemed to depend on parameters such as jet frequency, velocity, slot/orifice size and possibly fluid viscosity. The observations of Mittal *et al.* (2001) suggested that vortex dipoles are expelled if the self-induced velocity (V_I) of the dipole is greater than the jet ingestion velocity (V_j). Using simple scaling arguments to estimate this self-induced velocity, the following criterion for jet formation was put forth: jet formation requires that $V_I/V_j \sim V_j/(\omega_j d) > K$ where V_j is a mean jet exit (or ingestion) velocity, ω_j is the angular frequency of the jet, d is the jet width and K is an $O(1)$ constant. If we denote $f_j d/V_j$ as a jet Strouhal number (St) then the above criteria can be written as $St < K/2\pi$. Independently, Smith & Swift (2001) also arrived at a similar criterion although their criterion was based on the non-dimensional stroke-length which is also related to the jet Strouhal number (Holman *et al.* 2005). This criteria was subsequently subjected to extensive validation and refinement by Utturkar *et al.* (2003) and Holman *et al.* (2005), and found to be valid over a whole range of synthetic jet designs. This confirmed the basic validity of the scaling analysis and the underlying flow physics. It further indicated that the vortex strength and celerity were all governed by the jet Strouhal number St. This parameter was therefore expected to be singularly crucial in determining the downstream evolution of the synthetic jet.

Other numerical simulations of note are by Lee & Goldstein (2002) who reported two-dimensional computations of an array of synthetic jets performed using an immersed boundary method. Ravi, Mittal & Najjar (2004) used direct numerical simulations to study the effect of slot aspect-ratio on the formation and evolution of synthetic jets in quiescent and non-quiescent external flow. In the case of jets formed from rectangular slots in quiescent external flow, they observed the phenomenon of axis-switching in the jets similar to continuous jets due to self-induction of the vorticity field. For a fairly comprehensive review of both the experimental and computational investigations, see Glezer & Amitay (2002).

In the study reported here, the unsteady evolution of a synthetic jet in an otherwise quiescent external flow is investigated by time-accurate three-dimensional simulations of incompressible Navier–Stokes equations. The simulations are intended to model the experimental configuration of Yao *et al.* (2004*b*) who performed a detailed experimental investigation of a piezoelectric-diaphragm-driven synthetic jet. The details of the experimental configuration will be discussed in the next section. The key features of the experiment were that the jet has a large aspect-ratio rectangular slot and the operational parameters of the jet were such as to produce a synthetic jet that transitions to turbulence in the external quiescent flow. This point will be emphasized later in the paper. The experiments used hot-wire, laser-Doppler and particle-image velocimetry to quantify the jet flow, and the comprehensive set of available experimental data is used to validate the current simulations. Beyond this, in the current study we use the computed results to explore the vortex dynamics and the unsteady characteristics of the flow both outside and inside the jet cavity. It should be noted that there are virtually no reliable data available for the flow inside the jet slot and the cavity. Such data are, however, extremely useful in the context of actuator design and the development of low-dimensional models for these actuators (Gallas *et al.* 2004*a*). Thus, we expect that the current data will find use in these arenas as well as serve as a complementary database for future validation studies. A number of different groups attempted to compute this flow using a variety of techniques ranging from direct-numerical simulations to Reynolds-averaged Navier–Stokes (RANS) computations and Rumsey *et al.* (2004) have provided an overview of these simulations.

The paper is organized as follows. We begin by describing the experimental configuration and the computational model that is used in the current study. Following

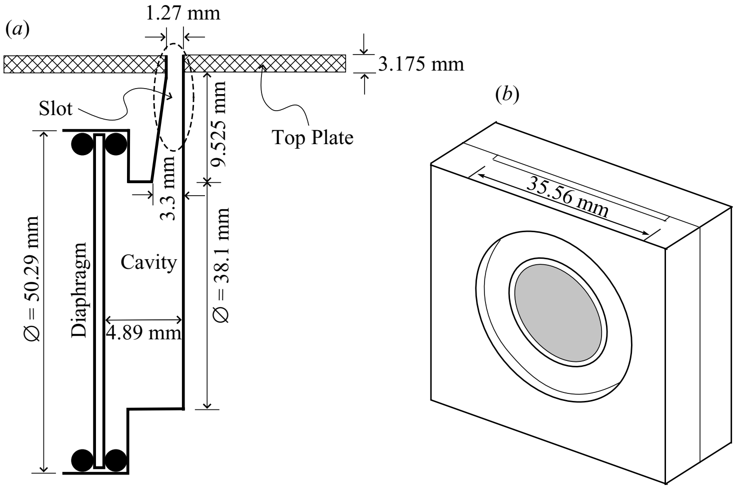

Figure 1. (*a*) Cross-sectional schematic of the jet configuration used in the experiments (not to scale). The dashed oval indicates roughly the region of the jet actuator modelled in the current computations. (*b*) Engineering drawing of actuator geometry used in the experiments.

this we present computed results for the outer jet flow including streamline plots, vortex visualizations, and time- and phase-averaged velocity profiles. These results are compared to the available experimental data in order to examine the fidelity, accuracy and limitations of the current computational model as well as to assess the effect of grid resolution and computational domain size on the computed results. Phase- and time-averaged velocity profiles are then presented for the flow inside the jet slot and cavity, and used to examine the flow development in these regions. Finally, we examine the temporal dynamics and turbulence characteristics of flow inside as well as outside the jet cavity by plotting and analysing time series and corresponding spectra.

2. Simulation overview

2.1. *Experimental jet configuration*

Figure 1(*a*) shows a cross-sectional side-view schematic of the synthetic jet actuator used in the experiments, whereas figure 1(*b*) shows a drawing of the overall actuator geometry. The side-view schematic is not to scale, but does show the salient features and dimensions of the geometry. The cavity is essentially cylindrical in shape and relatively thin in the horizontal direction. Furthermore, the circular piezoelectric diaphragm is mounted on one sidewall of the cavity and this leads to a highly non-symmetric cavity configuration. In addition, the jet slot has an unsymmetric taper with a taper angle of approximately 12°. The exit of the jet slot is rectangular in shape and has a width of 1.27 mm and lateral dimension of 35.56 mm.

The drive frequency (f_D) of the diaphragm used in the experiments of Yao *et al.* (2004*b*) is 444.7 Hz, and is close to the natural frequency (f_N) of the diaphragm, which is estimated from the linear composite plate theory by Gallas *et al.* (2004*b*) to be 460 Hz for a clamped circular diaphragm. Using their lumped element models (Gallas *et al.* 2003*a*) of these actuators, Gallas *et al.* (2003*b*) have made a convincing case that when the natural frequency of the diaphragm and the drive frequency are significantly less than the Helmholtz frequency of the cavity/orifice, compressibility effects do not play a significant role in determining the jet output. These lumped element models have also been used successfully for predicting the jet output for a variety of synthetic jet actuators including the actuator used in the experiment of Yao *et al.* (2004*b*). For this actuator, the model of Gallas *et al.* (2004*b*) predicts a Helmholtz resonant frequency (f_H) of the cavity to be about 1911 Hz. It further indicates that compressibility effects on the jet output are negligible for diaphragm frequencies less than about 700 Hz. Thus at the operating frequency of 444.7 Hz, the response of the fluid in the jet cavity is expected to be essentially incompressible. Coupling this with the findings of Utturkar & Mittal (2002) that in the incompressible regime, the shape and size of the cavity and the orifice, and diaphragm placement have little effect on the jet characteristics, we hypothesized that the external jet characteristics could be matched by performing an incompressible simulation with a simpler equivalent cavity configuration that matches certain dimensionless parameters, as discussed below.

Another key aspect of the jet is its aspect ratio. For the current jet, the aspect ratio is 28 which is quite large. With this large aspect ratio, the experimentalists expected that the flow, at least in the central region up to some distance from the jet exit would be unaffected by end-effects and would consequently, be nearly homogeneous in the spanwise direction. Consequently, most of the flow measurements were made at the central spanwise plane and they even recommended that two-dimensional simulations be used to model this region of the flow. In general, experiments performed for any nominally two-dimensional shear flows such as wakes, jets and shear layers will be subject to end-effects. These effects can be mitigated by choosing a large spanwise aspect ratio or by other endwall treatments, but they can never be fully eliminated. End-effects typically grow away from the endwalls in the downstream direction and will eventually effect the entire flow at some downstream distance. Thus, in attempting to computationally model the homogeneous region of such flows it is important to understand fully the extent of the end-effects. For the current flow, this is even more the case since end-effects manifest themselves through a strong axis-switching phenomenon (Ravi *et al.* 2004) whereby the rectangular vortex structures emanating from the jet deform as they convect downstream and essentially orient their long axis perpendicular to their initial orientation.

Measurements of the spanwise variation of the jet provided to us by Yao *et al.* (2004*a*) and shown in figure 2, provide a clear view of this phenomenon. The figure shows contours of time-averaged streamwise velocity on the $x_1 = 0$ plane along the length of the slot (see §§ 2.2 for the definition of the coordinate system). In this figure, the centre of the slot is at $x_3 = 0$ and the left-hand edge is at about $x_3 = -18$ mm. The figure clearly shows that edge-effects rapidly intrude into the central part of the jet. Although the precise spanwise width and vertical extent of this homogeneous core are difficult to estimate from these data, it is clear that this region of the jet does not extend much beyond a distance of about $x_2 \approx 8$ mm or $x_2/d \approx 6$. Thus, any computational model that attempts to model the homogeneous core flow of this jet cannot expect to match the experiments beyond this distance. Conversely, however, this also implies that a carefully performed spanwise homogeneous simulation should be able to match the experiment up to about this distance and provide a detailed view of the jet characteristics in the homogeneous core region of the jet. This is indeed the objective of the current computational study.

2.2. *Computational jet configuration*

Based on the above reasoning, a very simple actuator configuration was chosen for the computational study (figure 3). The origin of the coordinate system is fixed in

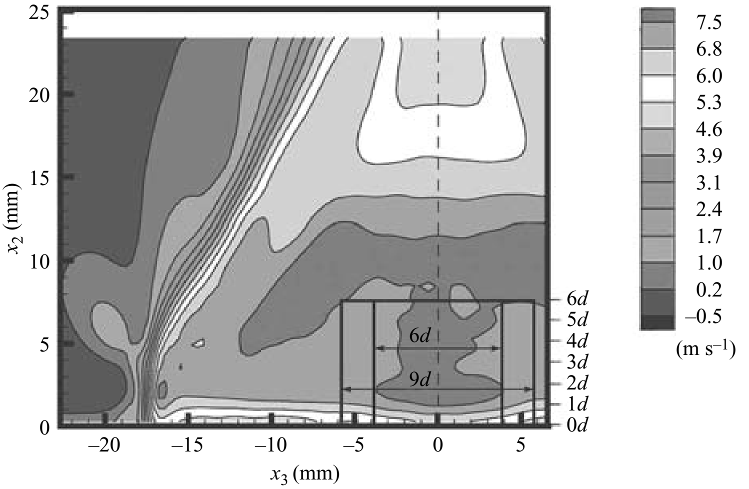

FIGURE 2. Time-averaged streamwise velocity measured on the $x_1 = 0$ plane by Yao *et al.* (2004*a*).

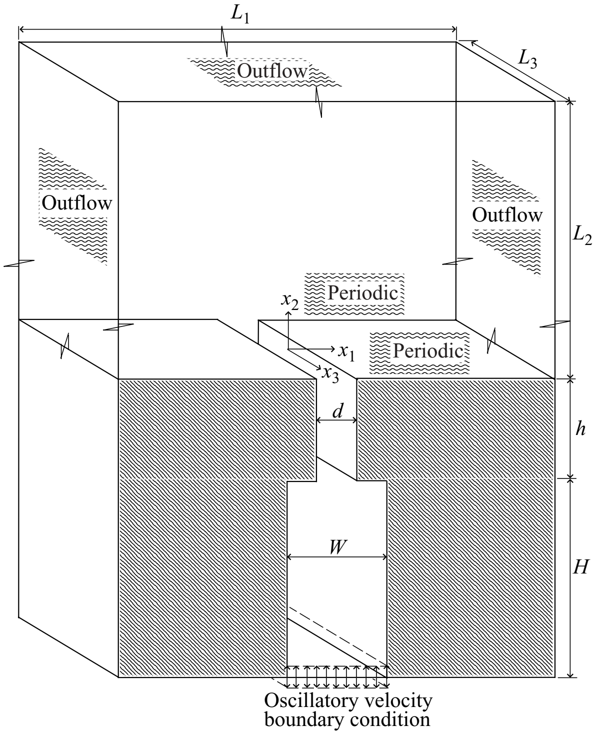

FIGURE 3. Schematic of the jet configuration and computational domain used in the numerical simulations (not to scale).

the jet exit plane at the centre of the orifice. Note that x_1, x_2 and x_3 are in the cross-stream, streamwise and spanwise directions, respectively. The cavity is assumed to be a rectangular box of width W and height H. Similarly, a rectangular jet slot of width d and height h is employed. In the spanwise (x_3) direction, we assume the flow to be homogeneous and consistent with this approximation, the entire geometry was assumed to be invariant in this direction. In practice, a finite spanwise domain size L_3 was chosen and periodic boundary conditions applied at these spanwise boundaries.

The entire actuator geometry can therefore be defined in terms of the following four non-dimensional parameters: cavity aspect ratio (H/W), slot height-to-width ratio (h/d), cavity-to-slot width ratio (W/d) and slot spanwise aspect ratio (L_3/d). For the current simulations, the first three are fixed at values of 2.0, 2.6 and 2.45, respectively. Four different spanwise aspect ratios ranging from $3d$ to $9d$ are employed in order to examine the effect of this parameter on the flow, and this issue will be discussed further in a later section of the paper. Note that the initial intent was to match some of these parameters to the experiment. However, the vast differences in the two geometries and the highly complex actuator topology made this task virtually impossible. Thus, in the end, the geometry was chosen so as to minimize, as far as possible, the demands on the grid generation and the computer processing time required for these expensive simulations.

Note that with the normalized dimensions chosen as above, the computational jet configuration essentially models only the slot region of the jet indicated by a dashed oval in figure 1(*a*). Thus, none of the experimental jet cavity below the slot or the region containing the diaphragm is included in the simulations. Furthermore, we represent the continuously expanding experimental slot with a simple geometry that has a sudden expansion with an expansion ratio that is nominally representative of the experimental configuration. Since we are only modelling the experimental slot in the simulations, we also employ a simple velocity boundary condition at the lower horizontal boundary of the computational jet cavity which is of the form $[u_1, u_2] = [0, V_0 \sin(2\pi f_j t)]$ where V_0 is the velocity amplitude and f_j the oscillation frequency. This boundary condition essentially provides a simple sinusoidal representation of the mass flux produced in the slot by the motion of the diaphragm. Again, this simple boundary condition is in line with our previous assertion that we do not expect the external flow to be sensitive to these details inside the jet cavity.

The jet emanating in the x_2-direction from the type of jet configuration chosen can be characterized in terms of a jet velocity (V_j), jet width (d), jet frequency (f_j) and fluid kinematic viscosity (ν). The jet velocity V_j can be characterized in different ways, but in the current study we use the mean exit velocity during the expulsion portion of the cycle as the characteristic jet velocity. Thus, V_j is defined as

$$V_j = \frac{2}{AT} \int_0^{T/2} \int_A u_2^e(x_1, x_3, t)\, \mathrm{d}A\, \mathrm{d}t,$$

where $u_2^e(x_1, x_3, t)$ is the x_2-component of the velocity at the exit plane of the jet slot, A is the cross-sectional area of the slot and $T = 1/f_j$ is the time period of the synthetic jet cycle.

Dimensional analysis indicates that there are two independent non-dimensional parameters that characterize the external jet. A convenient two-parameter set consists of a jet Reynolds number Re and a jet Stokes number S defined as

$$Re = \frac{V_j\, d}{\nu}, \qquad S = \sqrt{\frac{2\pi f_j\, d^2}{\nu}},$$

respectively. Thus in order to achieve dynamic similarity between the simulations and experiments, matching of these two parameters is required. It should be noted that $Re/S^2 = V_j/(2\pi f_j d) = (2\pi St)^{-1}$ and therefore matching of the Reynolds and Stokes

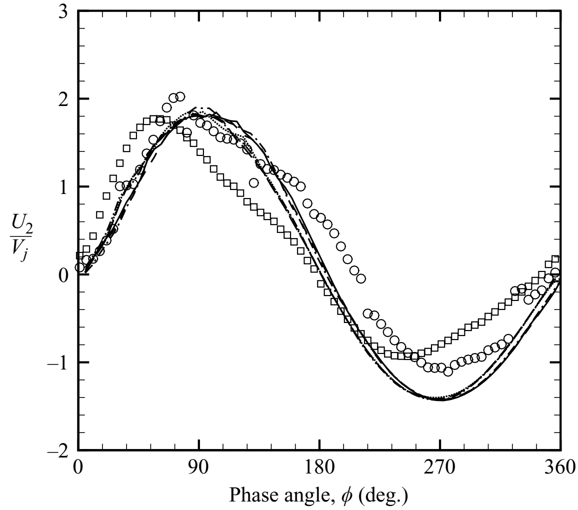

FIGURE 4. Phase-averaged time history of streamwise velocity U_2/V_j at $x_1/d = 0$ and $x_2/d = 0.1$. —·—, Case 1; - - -, Case 2; —··—, Case 3; ——, Case 4; — — —, Case 5; ···, Case 6; ○, PIV; □, LDV.

numbers also ensures matching of the jet Strouhal number St which is a crucial parameter in this flow (Utturkar *et al.* 2003; Holman *et al.* 2005).

Given the jet frequency, jet width and kinematic viscosity of air, we estimate the Stokes number for the jet in the experiments to be 17.0. The jet Reynolds number, however, is more difficult to estimate accurately since it requires knowledge of the spatial and time mean exit flow velocity. This quantity was not measured in the experiment and we have therefore estimated this from the available experimental data. Figure 4 shows the experimental measurements of the phase-averaged time history of the vertical velocity U_2, along the centreline at $x_2/d = 0.1$, obtained by Yao *et al.* (2004*b*) using PIV and LDV. It can be observed from this figure that there is significant variability between the measurements obtained using two different techniques with respect to peak-to-peak variation and alignment in phase, largely attributed to actuator ageing effects (Yao *et al.* 2004*a*). Because of physical limitations, experimental measurements could not be made at the jet exit plane (i.e. at $x_2/d = 0$), with the plane at $x_2/d = 0.1$ being the closest one. The PIV dataset is the most comprehensive dataset available from this experiment and, based on these data, we estimated that the V_j for this jet was about 14 m s^{-1}. The chosen value of V_j then leads to a jet Reynolds number of 1150. This implies that $Re/S^2 = 3.97$ and the jet Strouhal number is about 0.04 and thus, based on the jet formation criterion mentioned before, we expect the formation of a strong jet. It should, however, be noted that the uncertainty inherent in our estimate of V_j translates into a corresponding uncertainty in the jet Reynolds and Strouhal numbers. Smith & Swift (2001) and Holman *et al.* (2005) have indicated that the Strouhal number, in particular, has a significant effect on the jet formation and evolution. Uncertainty in the Reynolds number could also potentially have an effect on our ability to compare with the experimental flow. In § 3.1, we examine the effect of the key parameters on the computed flow in order to assess the sensitivity of the external flow on these parameters.

In the current incompressible simulations, the amplitude of the velocity at the bottom boundary V_0 is related to the V_j through mass conservation by

$V_j = (2V_0/\pi)(W/d)$. Thus, V_j can be prescribed by applying a suitable value of V_0. In the current simulations, V_j is set to 1.0 for convenience. Similarly, d is set to a value of 1.0. The frequency f_j and kinematic viscosity can now be chosen in the simulations to match the other two parameters Re and S. Figure 3 also shows the boundary conditions applied on the outer domain boundaries. An outflow velocity boundary condition is prescribed on the east, west and north boundaries to allow the flow and vortex structures to exit the domain with minimal reflections. Periodic boundary conditions are prescribed in the spanwise (x_3) direction. As mentioned earlier, this periodicity in the span is intended to model the spanwise homogeneous flow in the central region of the experimental jet.

2.3. *Data reduction*

The various averaging operations employed in the computation of flow statistics in the current study are described as follows along lines similar to Mittal, Simmons & Najjar (2003). For a generic flow variable $f(\boldsymbol{x}, t)$, the spanwise-averaged time-mean over M cycles is defined as

$$\langle f \rangle (x_1, x_2) = \frac{1}{L_3} \frac{1}{MT} \int_{t_0}^{t_0+MT} \int_{-L_3/2}^{L_3/2} f(\boldsymbol{x}, t) \, \mathrm{d}x_3 \, \mathrm{d}t,$$

where t_0 corresponds to the initial time of the averaging process. Deviation from the time-mean is computed as

$$f'(\boldsymbol{x}, t) = f(\boldsymbol{x}, t) - \langle f \rangle.$$

In addition, for flows with imposed periodic forcing such as the one under investigation here, it is useful to compute a phase average (Reynolds & Hussain 1972). The spanwise-averaged phase-mean over M cycles is defined as

$$F(x_1, x_2, t) = \frac{1}{L_3} \frac{1}{M} \sum_{n=0}^{M-1} \int_{-L_3/2}^{L_3/2} f(\boldsymbol{x}, t + nT) \, \mathrm{d}x_3.$$

Deviation from this phase average is referred to as ‘turbulent’ fluctuation and is computed as

$$f''(\boldsymbol{x}, t) = f(\boldsymbol{x}, t) - F.$$

The phase average F represents the time-varying coherent (or deterministic) part of the flow and primarily contains time scales directly associated with the organized wave motion. The deviation from the phase average (f'') represents the non-deterministic motions. Therefore, this decomposition provides a means for extracting scales that are associated with the organized wave motion from a background field of finite turbulent fluctuations.

2.4. *Numerical methodology*

The formation of a ZNMF synthetic jet in quiescent external flow is modelled by three-dimensional unsteady incompressible Navier–Stokes equations in primitive variables (velocity and pressure), written in tensor form as

$$\frac{\partial u_i}{\partial x_i} = 0,$$

$$\frac{\partial u_i}{\partial t} + \frac{\partial u_i u_j}{\partial x_j} = -\frac{1}{\rho} \frac{\partial p}{\partial x_i} + \nu \frac{\partial^2 u_i}{\partial x_j \partial x_j},$$

where the indices, $i = 1$, 2 and 3, represent the x_1, x_2 and x_3 directions, respectively, t is the time, ν is the kinematic viscosity, p is the pressure and the components of the velocity vector $\boldsymbol{u}$ are denoted by u_1, u_2 and u_3. The Navier–Stokes equations are non-dimensionalized with the length scale d and velocity scale V_j, and discretized using a cell-centred, collocated (non-staggered) arrangement of the primitive variables $(\boldsymbol{u}, p)$. In addition to the cell-centre velocities $(\boldsymbol{u})$, the face-centre velocities $(\boldsymbol{U})$, are also computed. Similar to a fully staggered arrangement, only the component normal to the cell-face is calculated and stored. The face-centre velocity is used for computing the volume flux from each cell. The advantage of computing the face-centre velocities separately is discussed in the context of the current method in Ye *et al.* (1999). The equations are integrated in time using a two-step second-order-accurate fractional step method. In the first step, the momentum equations without the pressure gradient terms are advanced in time. In the second step, the pressure field is computed by solving a Poisson equation. A second-order Adams–Bashforth scheme is employed for the convective terms while the diffusion terms are discretized using an implicit Crank–Nicolson scheme which eliminates the viscous stability constraint. The pressure Poisson equation is solved with a Krylov-based approach. The solver uses weighted-averaging of second-order central-difference and second-order upwind schemes for the discretization of convective terms. The QUICK scheme (Leonard 1979) obtained by setting the normalized weight factor for the central-difference term to 1/8 is used in the present computations. Care has been taken to ensure that the discretized equations satisfy local and global mass conservation constraints as well as pressure–velocity compatibility relations. The numerical method and the associated flow solver have been validated in several flows by comparisons against established experimental and computational data. Details have been presented elsewhere (Najjar & Mittal 2003; Dong, Mittal & Najjar 2006).

Small time steps corresponding to 1/14 000 of the jet period are employed in the calculations. The three-dimensionality in the solution is instigated by introducing a small sinusoidal spatial perturbation of the order of 1 % of V_j in the x_3-component of velocity over a hundred time steps in the first cycle. Thereafter, the three-dimensionality is allowed to develop on its own through the inherent instabilities in the flow. The solution was allowed to evolve for over ten cycles to eliminate transient effects, and up to six subsequent cycles were used in the computation of flow statistics discussed in § 2.3. In a later section, we examine the convergence of the statistics and demonstrate that six cycles provide adequate statistical convergence for the region of interest.

3. Results and discussion

3.1. *Parameter sensitivity*

A set of three-dimensional simulations was carried out in order to assess the sensitivity of the synthetic jet flow field to variations in the Reynolds number, the Stokes number and therefore the Strouhal number. These simulations provide valuable insight into the large-scale vortex dynamics including vortex celerity over a range of parameters. In doing so, they also give us an idea as to the extent to which we can expect the uncertainty in our estimate of V_j to affect the computed flow and hence the comparison with the experiment. As such it is useful to present this study at this earlier stage of the paper since it provides context to the subsequent simulations and comparison with experiments.

These simulations were carried out on the same densest x_1–x_2 grid used in the regular simulations and details regarding the grid are provided in the next section. Since

Case	Re	S	St
P1	1150	12.00	0.020
P2	1150	17.00	0.040
P3	1150	22.00	0.067
P4	850	14.62	0.040

Table 1. Various cases considered in the parameter study.

Case	L_1/d	L_2/d	L_3/d	N_1	N_2	N_3
1	60	60	3.0	142	230	8
2	40	42.45	3.0	132	220	16
3	40	42.45	3.0	132	220	24
4	40	42.45	4.5	132	220	24
5	60	60	6.0	142	230	48
6	60	60	9.0	142	230	48

Table 2. Various computations reported in the current study. L_1, L_2 and L_3 denote the domain size in the x_1, x_2 and x_3 directions, respectively. N_1, N_2 and N_3 denote the number of cells in the x_1, x_2 and x_3 directions, respectively. $Re = 1150$, $S = 17$, and $h/d = 2.6$.

these simulations were intended to capture only the large-scale vortex dynamics in the near-field and their dependence on the parameters Re and S, all these simulations employed the smallest spanwise domain size of $3d$. Various cases considered in this parametric study are given in table 1. In cases P1, P2 and P3, Re is fixed at 1150 and S (and hence St) is varied around the nominal value of 17 used in the later simulations (see table 2). Conversely, in Case P4, both Re and S are varied from their nominal value, while the Strouhal number is maintained fixed at the nominal value of 0.04. Thus, we reduce the Reynolds number by about 25 % from its nominal value and vary S and St over a range of about ± 30 % and ± 50 %, respectively, from their nominal values. The simulations allow us to delineate precisely the effect of the key parameters and this is sometimes difficult to achieve in experiments. For instance, Smith & Glezer (1998) examined the vortex celerity and trajectory where variation in the jet parameter was induced by increasing the amplitude of the piezo diaphragm. This, however, simultaneously increases the jet Reynolds and Strouhal number proportionately while at the same time keeping the Stokes number the same.

One of the primary objectives of these simulations is to examine the impact that variation in the key parameters has on the flow and consequently on our ability to match the experimental results. In this regard, vortex celerity is a key factor since correct prediction of this feature is a necessary condition for matching the phase-averaged flow profiles in the experiment. In this study, we use phase-averaged results to track the vertical trajectories of the vortex pairs as a function of the phase angle to determine the celerity of the vortices. Since the vortex dipole expelled from the jet produces a localized streamwise jet along the centreline, an easy way to track the location of the vortex dipole is to track the local maximum in the vertical velocity on the jet centreline.

Figure 5(a) shows a typical set of profiles of streamwise velocity u_2/V_j along the jet centreline from Case P2 at several phases of the synthetic jet cycle. The local maxima in these profiles (shown by solid circles in figure 5a) are used to determine the streamwise position of the vortex dipole at the various phases. These data are then compiled for all four cases and presented in figure 5(b). A number of observations can

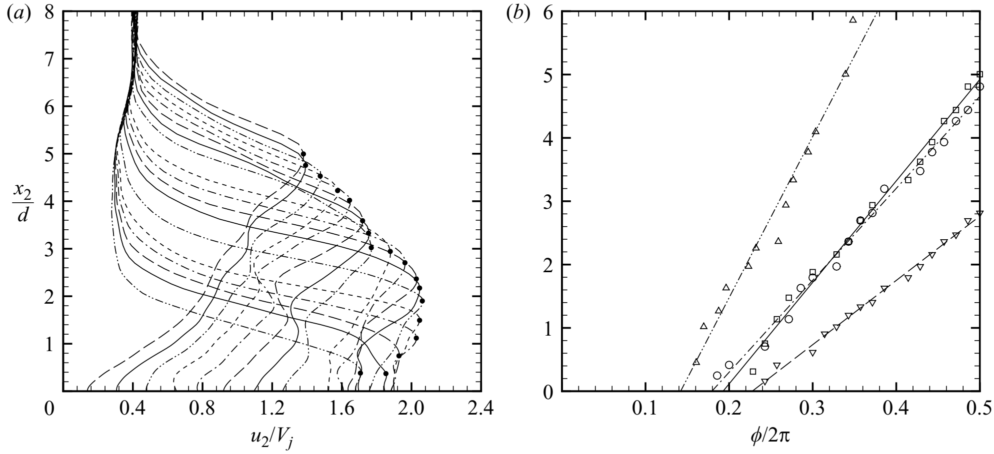

FIGURE 5. (*a*) Profiles of streamwise velocity u_2/V_j along the jet centreline at several phases of the synthetic jet cycle for Case P2. (*b*) Plot of streamwise position of vortex pairs as a function of phase-angle along with best-fit lines for various cases. △, Case P1; □, Case P2; ▽, Case P3; ○, Case P4.

be made from this figure. First, the vortex celerity which is directly related to the slope of the lines in this plot is nearly constant in the near field for each case. Secondly, the two cases P2 and P4 for which only the Strouhal numbers are the same, have nearly the same vortex trajectories and celerities. Note that the Reynolds numbers for these two cases are 1150 and 850, respectively, and the Stokes numbers are 17 and 14.62, respectively. This demonstrates that of all the parameters, the jet Strouhal number is the primary determinant of vortex celerity. The figure also shows that the vortex celerity decreases monotonically with increasing Strouhal number. Smith & Glezer (1998) noted that vortex celerity is directly proportional to the normalized stroke length L_0/d where $L_0 = V_j/2f$. In the current context, L_0/d is equal to $(2St)^{-1}$ and therefore the current results are generally in line with these experiments. However, as noted before, the current simulations allow us to clearly separate the Reynolds- and Strouhal-number effects and this was not possible in the experiments. Finally, the computational results also indicate that the formation time of the vortex, i.e. the time the vortex develops at the lip of the jet before convecting downstream, increases with increasing Strouhal number.

Examination of the velocity profiles for these various cases provides a more detailed view of the effect of these parameters on the flow and in figure 6 we show the velocity profiles for these four cases at a phase angle of 90°. Cases P1 and P3 produce velocity profiles that are vastly different from the other two cases, again underscoring the effect of the Strouhal number. On the other hand, the entire profiles for Cases P2 and P4 are similar despite the Reynolds number for Case P4 being 25 % less than that for Case P2. This, taken together with the observation regarding vortex celerity and trajectory, shows conclusively that even significant deviations in the Reynolds number have little effect on the near-field jet flow.

3.2. *Grid and domain sensitivity*

The various grids for which results are presented in the current paper are shown in table 2, and figure 7 shows different views of the typical mesh topology used in the current simulations. All the grids used are non-uniform in both the x_1- and

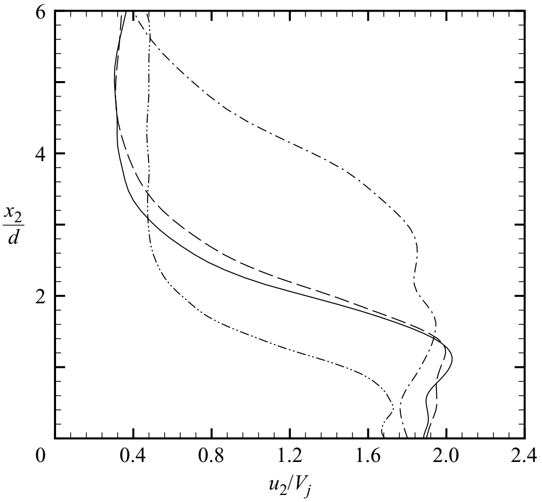

FIGURE 6. Profiles of streamwise velocity u_2/V_j along the jet centreline at peak expulsion $\phi = 90°$ for cases P1–P4. —·—, Case P1; ——, Case P2; —··—, Case P3; – – –, Case P4.

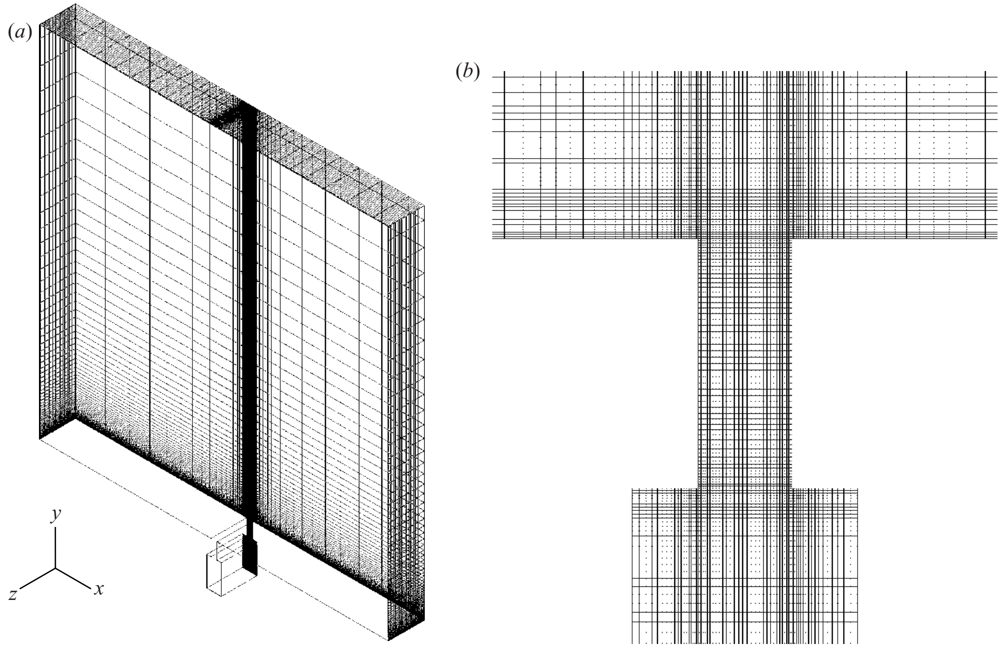

FIGURE 7. Typical computational mesh used in the simulations. (a) Overview of grid and domain used (only every other mesh point in each direction is shown). (b) Grid in the slot region.

x_2-directions, and uniform in the spanwise (x_3) direction. Sufficient clustering is provided in the slot-region along the x_1- and x_2-directions to resolve the vortex structures that form at the slot exit as well as the boundary layer in the slot. A typical grid has 32×55 ($N_1 \times N_2$) grid points in the slot. In arriving at the nominal grid which is used here, we performed a number of relatively inexpensive two-dimensional simulations. The grid resolution and domain size were increased systematically in each successive simulation and the baseline 132×220 grid and $40d \times 42.45d$ domain size selected was the one for which results from the two-dimensional simulations were found to be relatively insensitive to these aspects in the vicinity of the slot.

Although two-dimensional simulations are a reasonable way of assessing the grid and domain sensitivity of the computed solutions, it is nevertheless important to examine these effects in the three-dimensional simulations also. In particular, spanwise domain size and grid resolution effects can only be examined in the three-dimensional simulations. Furthermore, since the spreading rate of the jet is expected to be affected by the presence of three-dimensionality, it is also important to reassess the effect of domain size on the simulation results. Simulations on the different grids indicated in table 2 allow us to examine all of these effects. In particular, Cases 1 to 3 allow us to examine the effect of spanwise resolution, whereas Cases 3 to 6 provide an assessment of the effect of spanwise domain size. Finally, comparisons between Cases 4 and 5 also highlight the effect of outer domain size on the computed flow. As shown by Mittal & Balachandar (1997), Kaltenbach *et al.* (1999) and others, evaluation of the effect of spanwise domain size is crucial for such free-shear flows since such flows have strong spanwise instability mechanisms that can only be captured accurately if the spanwise domain size is large enough.

Results from Cases 1 to 6 are shown whenever a comparison of the velocity profiles along the jet centreline are made with experiments. This allows for a comprehensive evaluation of grid and domain sensitivity. Plots of the phase-averaged time history of the streamwise component of velocity U_2/V_j obtained from the simulations at $x_2/d = 0.1$ along the jet centreline are shown in figure 4. Also included in this plot are the PIV and the LDV measurements of Yao *et al.* (2004*b*). Whereas the computed results show grid convergence, as noticed before, the PIV and LDV measurements show significant differences. Even though the PIV data align better with the computations at maximum-ingestion phase ($\phi = 270°$), the maximum-expulsion in the PIV measurements leads the computational results at this station by as much as 14° in phase. The peaks of the PIV and LDV show significant mismatch in phase. Furthermore, whereas the phase difference between peak ingestion and peak expulsion for the computational data is very nearly 180°, it is about 200° and 190°, respectively, for the PIV and LDV measurements. *A priori* there is no reason to expect such a large difference between these two measurements since both techniques have the potential for providing accurate results for this flow (Holman 2006). Based on discussions with the experimentalists (private communication with C. S. Yao, NASA Langley) it seems that the differences are possibly due to changes in the response of the piezo actuator over the time lapse between the different experiments. One feature that is, however, consistent among both measurements and computations is that the peak expulsion velocity at the centreline is higher than the peak ingestion velocity. This is in line with the observations of Mittal *et al.* (2001) that the velocity profile at ingestion is almost a ‘plug’ profile, whereas that during expulsion has a better defined peak at the centreline.

Figures 8(*a*) and 8(*b*) show plots of phase-averaged streamwise velocity U_2/V_j profiles along the jet centreline $x_1/d = 0$ above the jet exit plane at phase angles $\phi = 92.6°$ and $\phi = 272.6°$, respectively. At the maximum-expulsion phase ($\phi \approx 90°$), Cases 3, 5 and 6 show reasonable convergence, and the computed velocity profiles agree reasonably with the measurements beyond $x_2/d = 2$. However, closer to the jet slot, there is more noticeable disagreement between the computations and experiment. In particular, we note that the local maximum in the experimental velocity occurs at $x_2/d \approx 1.3$, whereas for the computations, it occurs at about $x_2/d \approx 1.0$. Closer

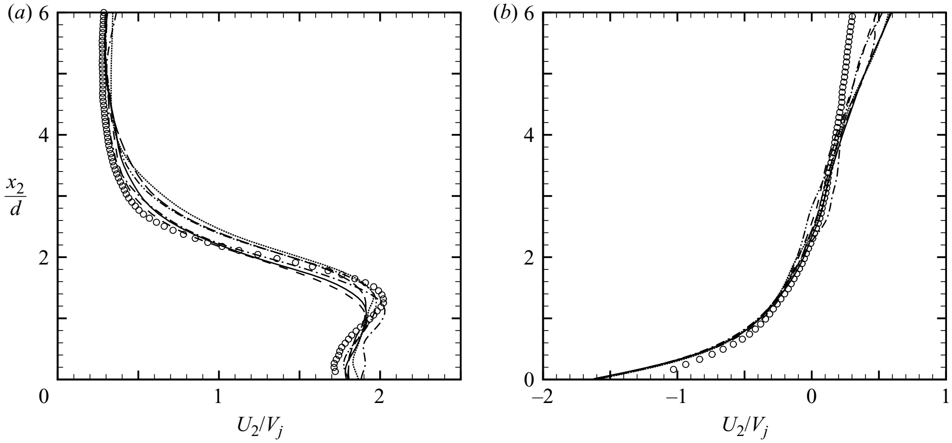

FIGURE 8. Phase-averaged velocity U_2 along the centreline $x_1/d = 0$. (*a*) Peak expulsion $\phi = 92.6°$ and (*b*) peak ingestion $\phi = 272.6°$. —·—, Case 1; ---, Case 2; —··—, Case 3; ——, Case 4; — — —, Case 5; ···, Case 6; ○, PIV (*a*) $\phi = 91°$ and (*b*) 271°.

examination of the profile indicates that this mismatch is consistent with the mismatch seen in figure 4 where the PIV data are seen leading the CFD data in phase during peak expulsion. This implies that the vortex expulsion process in the experiments leads that in the simulations and therefore the peak vertical velocity induced by the vortex pair will be further downstream in the experiment than in the computations.

At the maximum-ingestion phase ($\phi = 272.6°$), results from the computations match the measurements quite well until $x_2/d = 4$. Beyond this, all the simulations consistently deviate from the experiment. This has some interesting implications. Since all the computational results show the same trend, this suggests that the deviation from experiment is not due to grid-resolution effects, but rather is due to some inherent differences between the two configurations. Closer examination of the profiles indicates that between the six computations, the computed profiles from Cases 4, 5 and 6 more closely match each other. The key feature that distinguishes these three simulations from the first three is the spanwise domain size which is larger in Cases 4, 5 and 6. Note that Case 4 has a spanwise domain size of $4.5d$ whereas Case 6 has a spanwise domain that extends to $9d$. Two conclusions can be drawn from the fact that a two-fold increase in domain size produces similar results. First, the homogeneous core flow of the jet upto at least $x_2/d = 6$ can be captured only if the spanwise domain size is larger than $4.5d$, and secondly, that beyond about $x_2/d = 4$, end-effects start to intrude into the core of the jet. Thus, the homogeneous simulations will start to deviate from the experiment beyond this, irrespective of the spanwise domain size in the simulation. This is entirely consistent with the experimental observation (figure 2) as noted in § 2.1. Thus, in the rest of the paper, we limit our comparisons with the experiments only up to $x_2/d = 6$. Furthermore, since Case 5 seems to provide adequate results, we use data from this case for most of the analysis in this paper. It is worth noting that all computations were performed on a single 2.8 GHz Pentium® 4 processor-based workstation and the CPU time incurred for Case 5 was around 270 h per jet cycle.

3.3. *Vortex dynamics*

Contours of phase-averaged spanwise vorticity ($\Omega_3 d/V_j$) obtained for Case 5 are plotted in figure 9 as a function of phase angle ϕ for every 45°. Note that phase

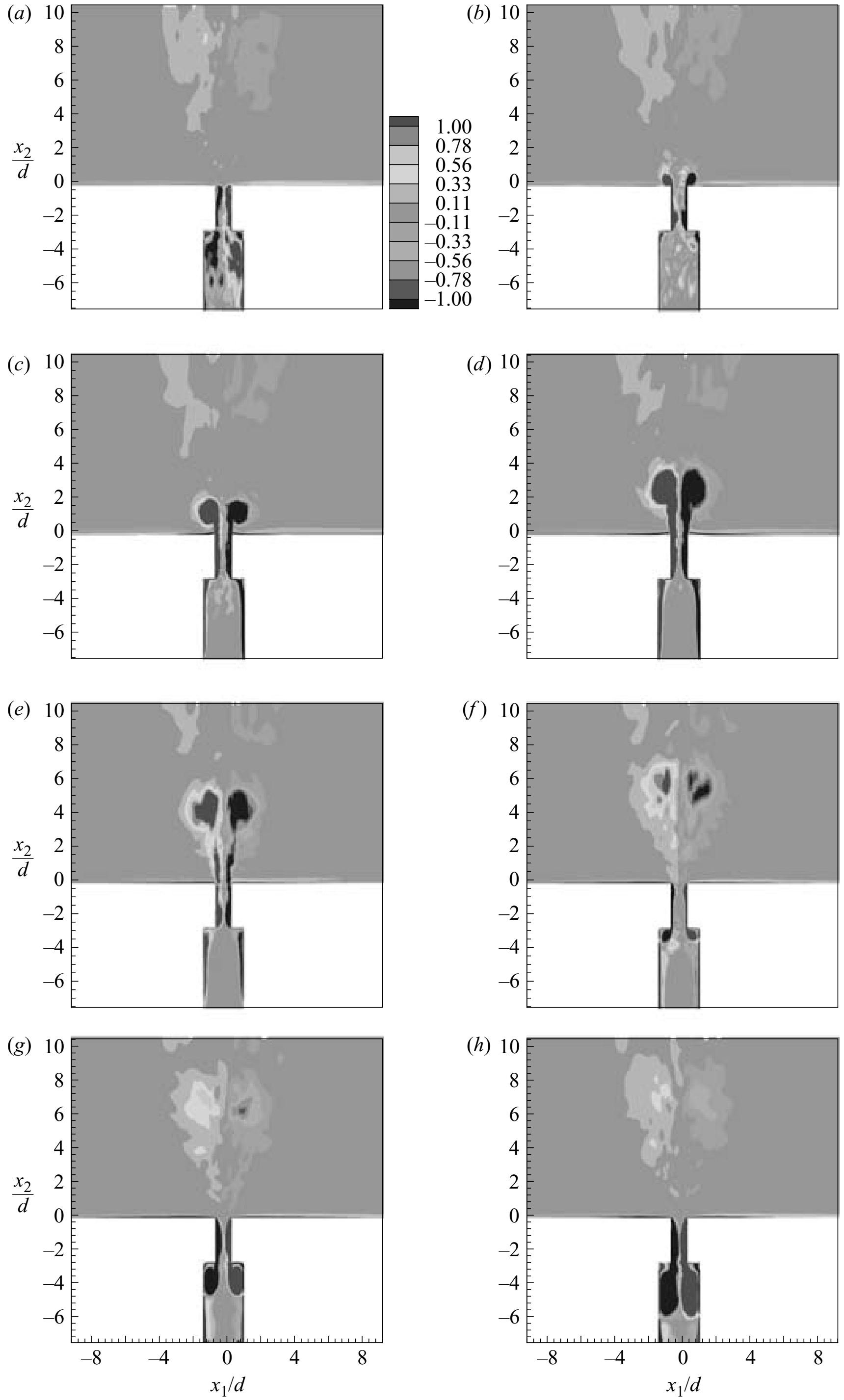

FIGURE 9. Sequence of contour plots of phase-averaged spanwise vorticity (Ω_3) non-dimensionalized by V_j/d at eight phases in the cycle for Case 5: (*a*) $\phi = 0°$, (*b*) $\phi = 45°$, (*c*) $\phi = 90°$, (*d*) $\phi = 135°$, (*e*) $\phi = 180°$, (*f*) $\phi = 225°$, (*g*) $\phi = 270°$ and (*h*) $\phi = 315°$.

angle $\phi = 0°$ is chosen to correspond to the commencement of the upward motion of the diaphragm modelled here by the oscillatory velocity boundary condition at the bottom of the cavity. Owing to the assumption of incompressibility, this also coincides with the start of the expulsion stroke. At $\phi = 0°$, the plot shows some remnants of the previous vortex pair in the near-field and the separation of the shear layer inside the slot at the exit, caused by the suction of the ambient fluid into the cavity before the upward motion of the diaphragm began. The plot also shows the presence of corner vortices in the cavity. At 45° in phase, a new vortex pair rolls up at the edges of the slot and its size is of the order of the slot width. Separation of the shear layer inside the slot entrance is also readily visible. When the roll-up process is completed at the maximum-expulsion phase of 90°, the vortex pair detaches from the exit plane and grows in size as it advects downstream. Note that this phase corresponds almost perfectly to the phase of the velocity profiles shown in figure 8(*a*), and the peak in the vertical velocity in this figure at about $x_2/d = 1$ is clearly seen to be due to the induced velocity of the vortex pair.

At $\phi = 135°$, the vortex pair has further developed in size and convected farther away from the slot. The expulsion phase is completed and the ingestion phase has commenced at $\phi = 180°$, by which time the vortex pair has advected sufficiently downstream (vortex core is roughly at $x_2/d \approx 4.5$) that it is not affected by the suction of ambient fluid into the cavity. From this point onwards, the convection speed of the vortex pair reduces and the vortex pair starts to lose its coherence and begins to mix with the ambient fluid. At $\phi \approx 225°$, the shear layers connecting the vortices to the slot have disappeared, and the suction initiates the formation of a vortex pair inside the cavity. At maximum-ingestion phase of 270°, the mixing of the primary vortex pair is mostly complete and as will be shown later, a fully developed turbulent flow exists beyond $x_2/d = 4$. The vortex pair inside the cavity, as seen at $\phi = 315°$, starts to grow in size while it descends into the jet cavity.

The above provides a qualitative view of the development of spanwise vortex structures. However, the flow is highly three-dimensional, and so it is useful to examine the three-dimensional vortex topology of this flow. In the current study, three-dimensional vortical structures are identified by plotting an isosurface of the imaginary part of the complex eigenvalue (λ_i) of the instantaneous velocity gradient tensor. This method of identifying vortical structures in three-dimensional flow fields has been suggested previously by Soria & Cantwell (1993) and has been used extensively for extracting vortical structures in the wakes of cylinders (Mittal & Balachandar 1997) and spheres (Mittal 2000). In this method, the vortical structures are identified as regions where rotation is dominant over the strain, and so they correspond to circular streamlines in planes normal to the axis of these structures.

Figure 10 depicts such isosurfaces obtained for Case 5 during the eighth cycle at $\phi \approx 90°$. The figure clearly depicts the process of transition of the primary vortex pair into a fully developed turbulent jet. At the maximum-expulsion phase of 90°, the plot shows the presence of spanwise-periodic counter-rotating rib-like vortical structures in the streamwise direction. These streamwise rollers coil around the cores of the primary vortex pair. As the primary vortex pair advects downstream in the subsequent phases, these spanwise instabilities undergo rapid amplification owing to three-dimensional vortex stretching leading to the breakdown of the primary vortex pair and complete mixing of the vortices with the ambient fluid within a short distance from the orifice. This process of transition is consistent with the phase-locked smoke visualizations of a synthetic jet at $Re = 766$ reported by Smith & Glezer (1998).

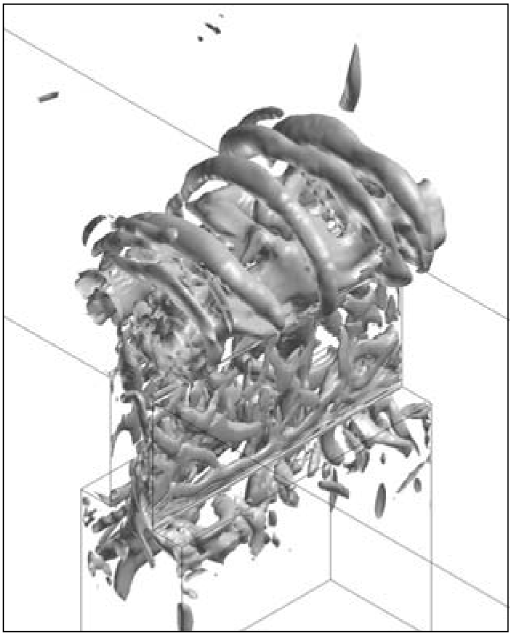

FIGURE 10. Vortical structures in the near-field for Case 5 at $\phi \approx 90^\circ$. The vortical structures are visualized by plotting one isosurface of λ_i corresponding to a value of 1.0.

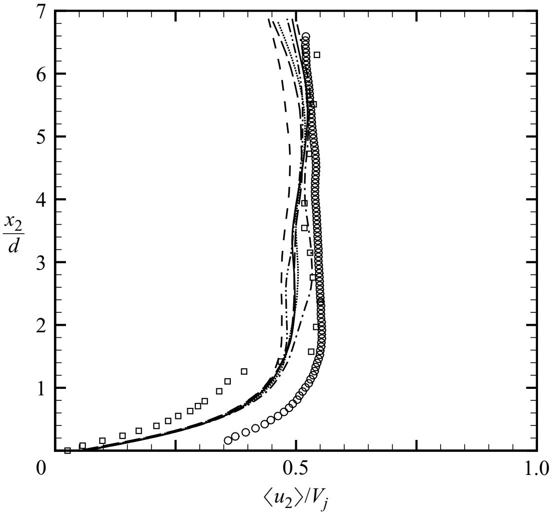

FIGURE 11. Plot of time-averaged streamwise velocity $\langle u_2\rangle/V_j$ along the centreline $x_1/d = 0$. —·—, Case 1; - - -, Case 2; —··—, Case 3; ——, Case 4; — — —, Case 5; ···, Case 6; ○, PIV; □, Hot-wire.

3.4. *Mean flow characteristics*

Figure 11 shows the computed time-averaged streamwise velocity profiles along the jet centreline above the jet exit plane. Also shown in this plot are the PIV and the hot-wire measurements of Yao *et al.* (2004*b*). There is a clear discrepancy between the PIV and the hot-wire measurements up to about $x_2/d = 1.5$. In particular, the PIV

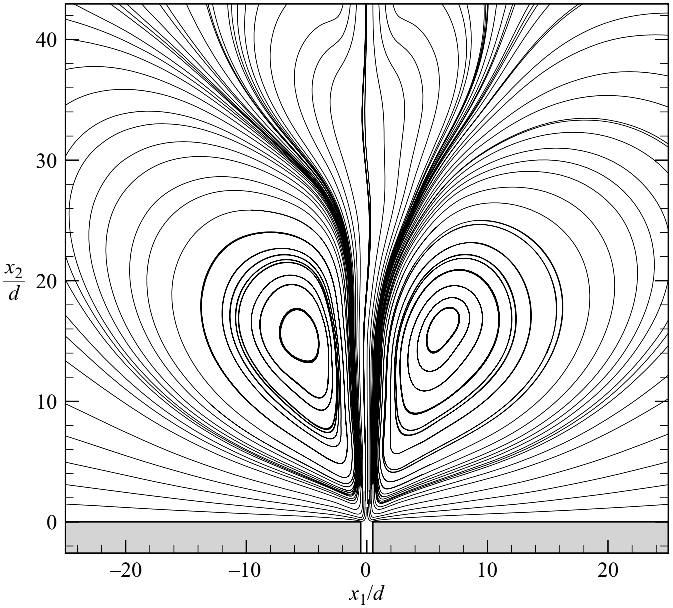

FIGURE 12. Plot of streamlines corresponding to time-averaged velocity field for Case 5.

data show significantly higher velocity than the corresponding hot-wire measurement. Furthermore, the PIV measurements show an unexpectedly large non-zero velocity at $x_2/d \approx 0$. In contrast, both simulations and the hot-wire measurements are in reasonable agreement near $x_2/d \approx 0$. Both datasets show a small non-zero velocity at $x_2/d = 0$ which is consistent with the nature of the flow profiles produced during expulsion and ingestion as discussed in a previous section of this paper. Beyond about $x_2/d = 1.5$, the two experimental measurements are consistent with each other. In this region, the simulations, although predicting the shape of the profiles reasonably well, under-predict the velocity magnitude. For instance at $x_2/d = 2$, the experiments indicate a normalized mean velocity of about 0.53, whereas the simulations predict a value of about 0.48. There is also a slight disagreement between the six simulations beyond about $x_2/d = 1.4$, although up to about $x_2/d = 4.0$ the difference is only about 5 % of the local value. Beyond this point, differences between the computed profiles increase to about 10 %, and this is probably due to the influence of spanwise confinement effects.

This time-mean plot also provides a good opportunity for us to evaluate the statistical convergence of the computed results. In order to accomplish this, we have computed the time-mean centreline velocity over 2, 4, 5 and 6 cycles for Case 5. Following this, we evaluate the maximum difference between each averaged profile and the profile obtained from averaging over 6 cycles. Up to a distance of $x_2/d = 6$ which is the region of comparison here, we find that the maximum deviation is equal to 0.020, 0.014 and 0.007 for averages accumulated over 2, 4 and 5 cycles, respectively. This indicates that the statistical variability in the velocity profiles averaged over 6 cycles is at most about 0.007 in the region of interest. This amounts to about a 1.4 % variation about the typical near-field value of 0.5 and indicates that 6 cycles provide adequate statistical convergence.

Figure 12 shows the streamlines corresponding to the time-averaged velocity field for Case 5. The plot shows a pair of relatively large recirculation regions on either

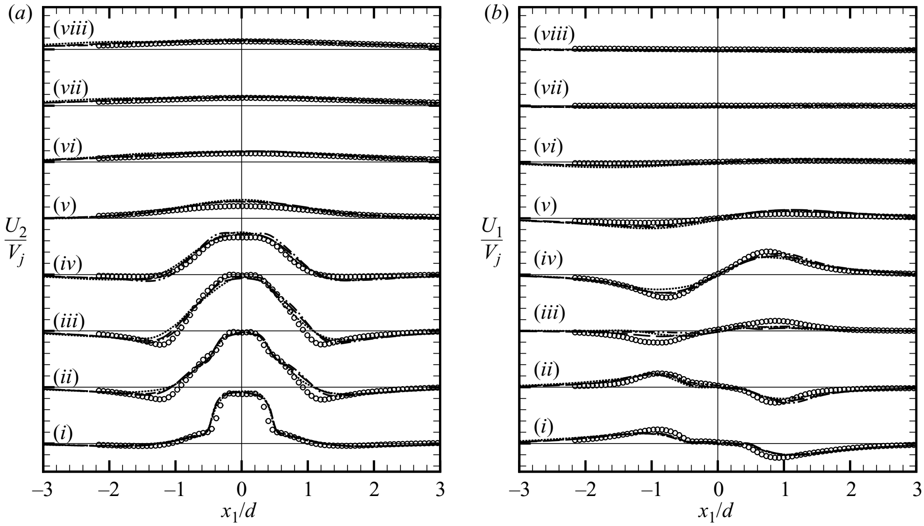

FIGURE 13. Cross-stream distributions of phase-averaged (*a*) streamwise U_2/V_j and (*b*) cross-stream U_1/V_j velocities at streamwise stations (*i*) $x_2/d = 0.5$, (*ii*) 1.0, (*iii*) 1.5, (*iv*) 2.0, (*v*) 3.0, (*vi*) 4.0, (*vii*) 5.0 and (*viii*) 6.0 at phase angle $\phi = 92.6°$. —··—, Case 3; ———, Case 5; ···, Case 6; ○, PIV $\phi = 91°$. Note that the major tick mark spacing on the vertical axis is $2V_j$.

side of the mean jet. The centres of these recirculation zones are roughly at a distance of 16*d* from the jet exit. Note that the formation of these recirculation zones is directly connected with the zero-net mass-flux characteristic of the synthetic jet since the mass flux in the central mean jet has to be balanced by a reverse flow towards the slot. Although the mean streamline pattern does not represent the motion of the fluid at any one time instant, it is indicative of convective time scales in the outer flow that are at least a magnitude (or more) higher than the jet time period. This has implications for computational modelling of these flows. Thus, although the near-field statistics converge rapidly, the presence of these large time scales indicates that large sampling times of the order of 100 cycles are probably required in any simulation or experiment that attempts to obtain accurate statistics for this outer region of the flow.

3.5. *Near-field jet flow*

Figure 13(*a*) shows comparisons with the measurements of phase-averaged streamwise velocity U_2/V_j above the jet exit plane at eight stations ($x_2/d = 0.5$, 1.0, 1.5, 2.0, 3.0, 4.0, 5.0 and 6.0) at $\phi = 92.6°$. Note that this phase is close to the maximum expulsion phase in the synthetic jet cycle. Furthermore, in these comparisons we include results from Cases 3, 5 and 6 which represent the entire range of spanwise domain sizes employed in the current study. At $x_2/d = 0.5$, the plot shows excellent agreement between the simulations and experiment wherein the simulations accurately predict the shape as well as the magnitudes. The profile itself shows three distinct regions in the jet at this location. First is the central jet core region that extends from $-0.5 < x_1/d < 0.5$ and contains fluid expelled from the jet slot. Extending approximately 0.5*d* on either side of the jet core is a region of entrainment which consists of ambient fluid that has been entrained by core flow in the jet. The third region is beyond $|x_1/d| = 1.0$ and consists of the reverse flow induced owing to the zero-net mass flux constraint that governs this large-scale motion in the flow.

At the next streamwise station at $x_2/d = 1.0$, the agreement between simulations and experiment is still good, and both simulations and experiments still show some indications of the three-layered jet profile. At the next three stations, $x_2/d = 1.5$, 2.0 and 3.0, the simulations under- or over-predict the central peak by about 10 %, but predict the profile shape reasonably well. As mentioned earlier with reference to figure 8(*a*), this lower value is most probably due to the slight mismatch in the phase of peak jet expulsion between experiments and simulations. At the three downstream stations of $x_2/d = 4.0$, 5.0 and 6.0, we find a significant reduction in the centreline velocity. This is because at this phase in the cycle, the vortices that are forming at the jet lip are still upstream of these stations (figure 9*c*) and therefore the induced velocity at these stations is relatively small. The comparisons between the simulations and experiments are found to be excellent at these three stations.

Figure 13(*b*) shows comparisons with the measurements of phase-averaged cross-stream velocity U_1/V_j above the jet exit plane at the same eight stations ($x_2/d = 0.5$, 1.0, 1.5, 2.0, 3.0, 4.0, 5.0 and 6.0) at $\phi = 92.6°$. At $x_2/d = 0.5$ and 1.0, the agreement between the experiment and simulations is good. As is seen from figure 9(*c*), these two stations are located below the spanwise vortices which are centred at around $x_2/d = 1.2$ at this phase in the simulations. At the next two stations of $x_2/d = 1.5$ and 2.0, there is a more noticeable mismatch between the experiment and computations. In particular, the simulations tend to consistently under-predict the peak crossflow velocity at this location. This is probably connected to the dramatic change in the profile shapes in going from $x_2/d = 1.0$ to 1.5 because the station $x_2/d = 1.0$ is below the vortex cores and $x_2/d = 1.5$ is above the vortex cores. A small mismatch in the location of the vortex can therefore have a relatively large effect on the velocity profile at this location. At the next four stations ($x_2/d = 3.0$, 4.0, 5.0 and 6.0) the simulation results are generally in good agreement with the experiments, although the peak velocity at $x_2/d = 3.0$ is over-predicted by the simulations by about 10 %.

Next, we examine the phase-averaged velocity profiles (figure 14) at phase angle $\phi = 272.6°$ which is close to the maximum ingestion phase in the simulations. For the ensuing discussion it is useful to point out that the phase-averaged spanwise vorticity contour plot corresponding to this phase is shown in figure 9(*g*) and that at this phase, the vortex cores are located at a distance of about 6.6d from the slot exit. The streamwise velocity profiles at the same eight stations ($x_2/d = 0.5$, 1.0, 1.5, 2.0, 3.0, 4.0, 5.0 and 6.0) at phase angle $\phi = 272.6°$ are shown in figure 14(*a*). The first set of profiles are at $x_2/d = 0.5$ and at this station we find that the predictions from the simulations match the experiments well for $|x_1/d| \gtrapprox 1$. In the region $|x_1/d| \lessapprox 1$, we find that although the shape of the velocity profile is predicted well, the simulations over-predict the suction velocity by about 15 % as compared to the experiment. Note that at this station, the simulations are very much in agreement with each other as well as the hot-wire measurements (see figure 11). Furthermore, it is this lower suction velocity magnitude in the PIV measurements that leads to a unexpectedly large positive time-averaged velocity at this location (see figure 11). Thus, it is possible that the discrepancies between simulations and PIV data are attributable to the uncertainties in the experimental measurements.

At the next four stations, the agreement between the simulations and experiments is reasonable beyond $|x_1/d| \gtrapprox 2$. For $|x_1/d| \lessapprox 2$, the experiments show a narrow and distinct region of higher velocity at the centre which is the flow produced by an earlier vortex dipole. On the other hand, although the simulations do indicate a similar shape and even predict the centreline value reasonably well, they over-predict the width of this region. At $x_2/d = 4.0$ and 5.0, the simulations predict the peak

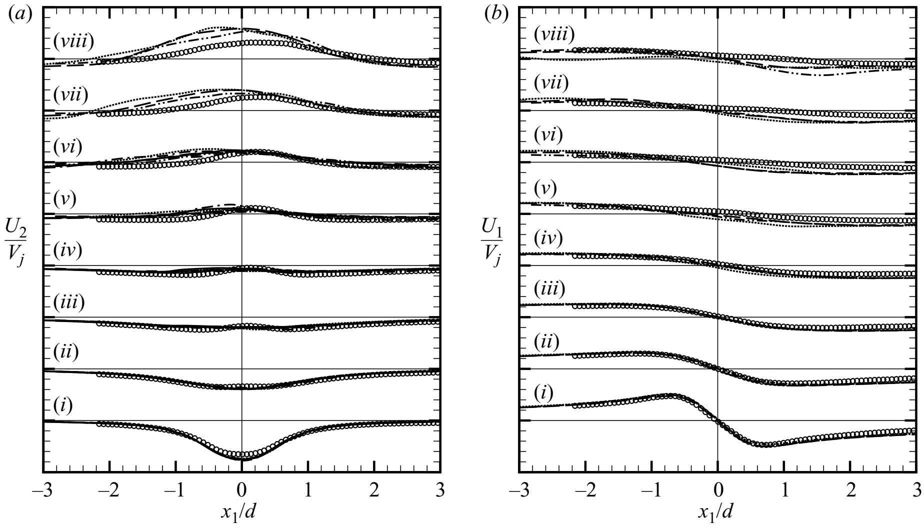

FIGURE 14. Cross-stream distributions of phase-averaged (*a*) streamwise U_2/V_j and (*b*) cross-stream U_1/V_j velocities at streamwise stations (*i*) $x_2/d = 0.5$, (*ii*) 1.0, (*iii*) 1.5, (*iv*) 2.0, (*v*) 3.0, (*vi*) 4.0, (*vii*) 5.0 and (*viii*) 6.0 at phase angle $\phi = 272.6°$. —··—, Case 3; ———, Case 5; ···, Case 6; ○, PIV $\phi = 271°$. Note that the major tick mark spacing on the vertical axis is V_j.

velocity fairly accurately, but the lack of symmetry in experimental profiles becomes readily apparent. As pointed out earlier, this slight asymmetry is probably due to the asymmetric jet slot used in the experiments. Finally, at $x_2/d = 6.0$ which is our most downstream station, we find that all the simulations are fairly consistent with one another, but notwithstanding the difference in symmetry, they clearly over-predict the peak velocity. This is again a clear indication that by this station, end-effects have intruded in the homogeneous core of the jet thereby making comparisons with the simulations difficult.

The cross-stream velocity profiles at these eight stations at this phase are shown in figure 14(*b*). The agreement at stations up to $x_2/d = 2.0$ is good. Beyond this, the difference due to the symmetry in the simulations becomes apparent. The simulations predict a somewhat larger cross-stream velocity outside the jet core, implying greater entrainment in the computed flow fields than that observed in the experiments. This is also connected with the lack of end-effects in the simulation which tend to reduce the entrainment in the (x_1, x_2)-plane. The prediction at $x_2/d = 6.0$, in particular, shows this effect clearly. From these phase-averaged profiles presented in figures 13 and 14, we note that the ratio of peak cross-stream to peak streamwise velocity at the jet exit is about 0.3 at maximum expulsion, whereas at maximum ingestion this ratio is about 0.6. The ratio at ingestion is higher because during ingestion, the velocity field at the jet exit resembles that of a sink which draws flow from all directions whereas during expulsion, the flow is mostly directed along the streamwise direction.

Figure 15(*a*) shows the cross-stream distributions of time-averaged streamwise velocity $\langle u_2 \rangle / V_j$ from the computations at the same eight stations ($x_2/d = 0.5$, 1.0, 1.5, 2.0, 3.0, 4.0, 5.0 and 6.0) above the jet exit plane. Also plotted are the corresponding profiles from the PIV measurements and the centreline velocity available from the hot-wire measurements. At stations $x_2/d = 0.5$ and 1.0, the computed velocity profiles closely match the PIV measurements outside the core region of the jet ($|x_1/d| \lessapprox 0.5$).

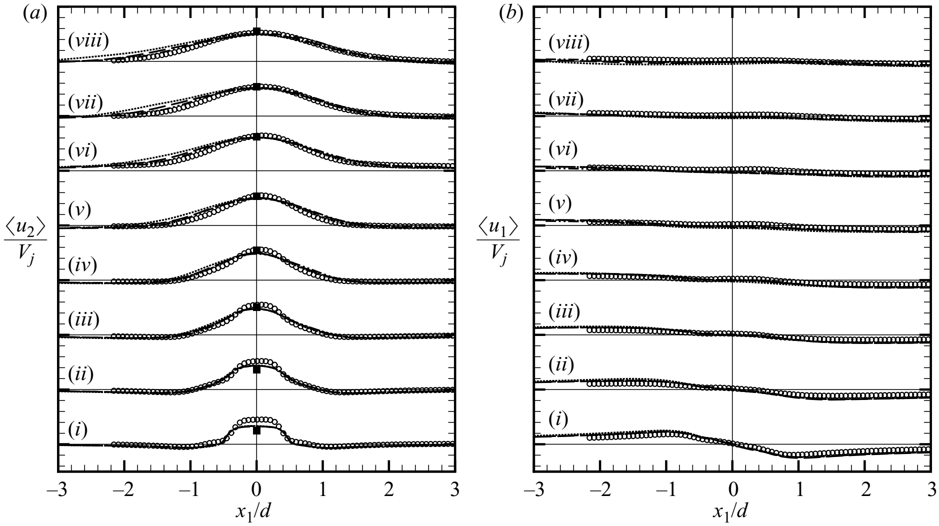

FIGURE 15. Cross-stream distributions of time-averaged (*a*) streamwise $\langle u_2 \rangle$ and (*b*) cross-stream $\langle u_1 \rangle$ velocities along the streamwise stations (*i*) $x_2/d = 0.5$, (*ii*) 1.0, (*iii*) 1.5, (*iv*) 2.0, (*v*) 3.0, (*vi*) 4.0, (*vii*) 5.0 and (*viii*) 6.0. —··—, Case 3; – – –, Case 5; ···, Case 6; ○, PIV $\phi = 91°$; ■, Hot-wire. Note that the major tick mark spacing on the vertical axis is V_j.

Within the jet core, however, the simulations predict a lower velocity than the PIV measurements; but, the hot-wire measurements at the centreline indicate an even lower velocity and the computed values are, in fact, between the PIV and hot-wire measurements. Thus, the prediction from the simulations is acceptable given the experimental uncertainty. Two other factors that probably have a bearing on the mean jet velocity near the jet exit are the nonlinear response of the diaphragm and the inherent uncertainty in choosing the jet Reynolds number for the simulations. The former (see figure 4) leads to a jet expulsion velocity in the experiments that is higher than in the simulations. The latter leads to uncertainty in the jet Strouhal number and hence the self-induced velocity of the vortices (Utturkar & Mittal 2002; Holman *et al.* 2005), and this can also directly affect the jet centreline velocity near the jet slot. A similar trend is observed at the six other downstream stations wherein the computed profiles are found to match the measured profiles reasonably well except near the jet centreline where the simulations continue to under-predict the velocity magnitude. Note that as we move downstream, the agreement between PIV and hot-wire measurements improves, which points to less experimental uncertainty in this region.

Figure 15(*b*) shows the cross-stream distributions of time-averaged cross-stream velocity $\langle u_1 \rangle / V_j$ at the same eight stations. In general, the agreement between simulations and experiment is good. The computed velocity profiles at the first five stations, however, consistently show slightly higher values than the measurements outside the core region of the jet, which again indicates a higher level of entrainment in the simulations than in the experiments.

The streamwise variation of the jet width is an important characteristic of the flow since it is dependent on the jet entrainment rate as well as the mixing inside the jet. In the current simulations we have defined the jet-width w_j (White 1991) as twice the cross-stream distance x_1 where the time-averaged streamwise velocity

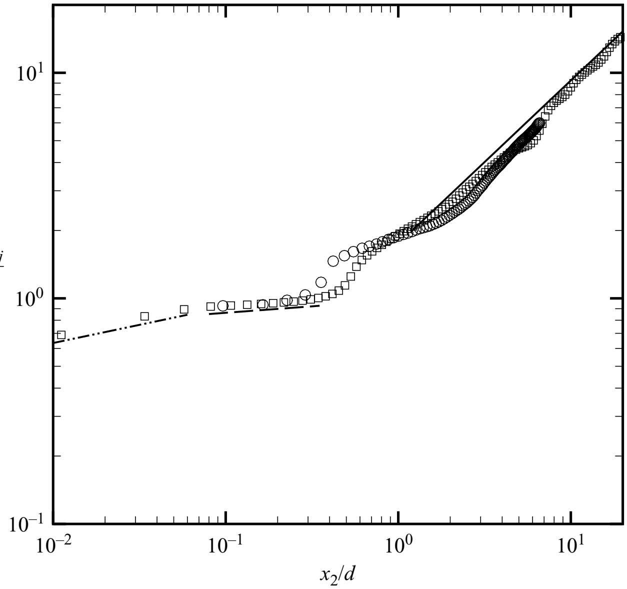

FIGURE 16. Plot of time-averaged jet-width w_j/d. □, Case 5; ○, PIV; —·—, $w_j/d \sim (x_2/d)^{0.16}$; - - -, $w_j/d \sim (x_2/d)^{0.06}$; ——, $w_j/d \sim (x_2/d)^{0.72}$.

$\langle u_2 \rangle$ is 1 % of the maximum or centreline velocity $\langle u_2 \rangle_{cl}$ (i.e. $\langle u_2 \rangle = 0.01\langle u_2 \rangle_{cl}$). This quantity has been estimated from both the PIV data and the Case 5 simulation, and compared in figure 16. The computed data indicate three distinct regions in the jet. The first region extends up to about $x_2/d \approx 0.07$ and in this region, the growth in the jet width is very small and the jet grows as $x_2^{0.16}$. The second region extends from $x_2/d \approx 0.07$ to $x_2/d \approx 0.25$ and in this region, the rate of the growth of the jet width is smaller than the growth in the first region. A best-fit line through the simulation data in this region indicates that the jet width in this region grows as $x_2^{0.06}$. These two regions of slow growth represent the developing regions of the jets. Beyond this region, both experiments and simulations indicate a more rapid growth in the jet width. The two data sets are in reasonable agreement with each other although the experiments exhibit more variability in jet-width with distance than the simulations. A best-fit line through the computed data shows that the jet in the outer region spreads as $x_2^{0.72}$. The jet width of a high-Reynolds-number continuous laminar jet emanating from a two-dimensional slot is known to increase as $x_2^{2/3}$ (White 1991) which is close to what we observe for the current synthetic jet. However, given that the current jet is oscillatory and at a relatively low Reynolds number, it is difficult to make any definitive statements regarding this comparison. It should be pointed out that Smith & Glezer (1998) made experimental measurements for a large (150) aspect-ratio synthetic jet at a jet Reynolds number (as defined in the current study) of 766 and found the streamwise growth of the jet width to scale as $x_2^{0.88}$. However, Smith & Swift (2001) carried out experimental measurements of synthetic jets with aspect ratios below 30 at higher jet Reynolds and lower Strouhal numbers (as defined in the current study) in the range of 1468–4400 and 0.006–0.037, respectively. They found jet growth rates that scaled as $x_2^{1.0}$ which is consistent with that of a continuous turbulent jet (Tennekes & Lumley 1972).

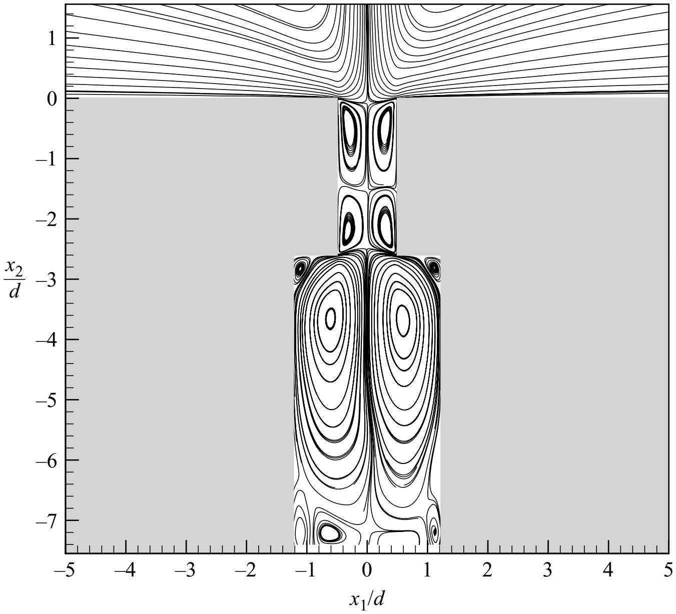

FIGURE 17. Plot of streamlines corresponding to time-averaged velocity field in the cavity for Case 5.

3.6. *Slot and cavity flow characteristics*

No measurements of the flow inside the jet slot or the cavity were made in the experiments of Yao *et al.* (2004*b*). Because of the difficulty of gaining non-intrusive access to the flow in these regions, no experiments to date have been able to make such measurements. However, it is useful to examine the computed flow in these regions in order to gain a better understanding of the actuator performance. The flow features in these regions also play an important role in the development of low-dimensional actuator models. Finally, accurate data on flow characteristics in these regions when combined with the data for the external flow, results in a comprehensive data set which can be used for numerical validation studies in the future. In this section, we discuss some key characteristics of the flow in these regions.

Figure 17 shows the streamlines corresponding to the time-averaged velocity field inside the slot and the cavity for Case 5. The mean velocity field inside the slot is characterized by two pairs of vortices, one at the slot entrance and the other at the slot exit. These vortex pairs are caused by the separation of the shear layers inside the slot at the entrance and at the exit during the expulsion and ingestion phases, respectively, of the synthetic jet cycle. Thus, nowhere inside the slot can the flow be considered fully developed and this has implications for the characterization of pressure drop across the slot (Raju *et al.* 2005). The mean flow field inside the cavity is characterized by corner vortices and a pair of large vortices that engulf the entire cavity. This large vortex pair in the mean field is generated as a result of the roll-up of the shear layer inside the cavity during the ingestion phase of the cycle.

The pressure drop across the jet slot and its relationship to the slot configuration and flow characteristics is a key component in the development of low-dimensional actuator models. For instance, the lumped-element model of Gallas (2005) attempts to predict the output velocity of ZNMF actuators, given the actuator design and operational parameters. In this context it is useful to examine the pressure drop

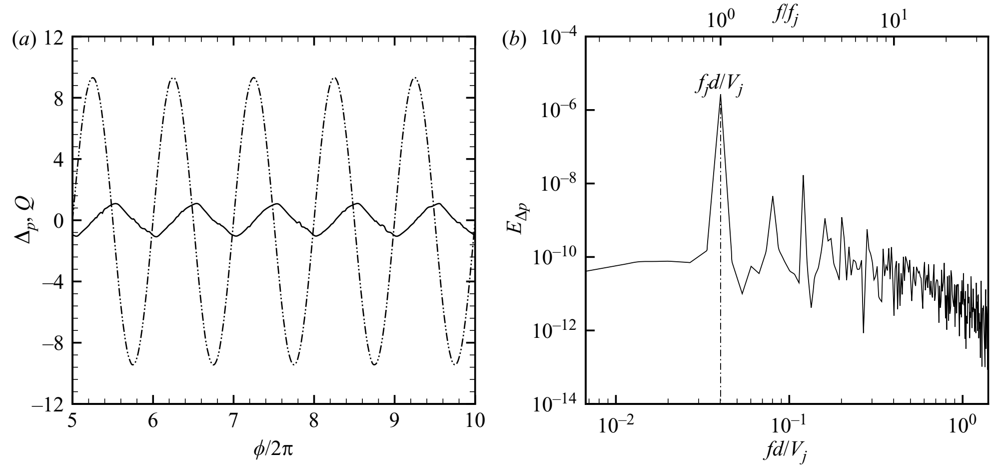

FIGURE 18. (*a*) Temporal variations of pressure drop and volume flow rate across the slot for Case 5. ———, Δp; —··—, Q. (*b*) Frequency spectra corresponding to temporal variation of Δp.

across the slot for the current configuration, and extract information that could aid the development and validation of such low-dimensional actuator models.

Figure 18(*a*) shows the temporal variation of the non-dimensional volume flow rate Q and the non-dimensional pressure drop Δp across the slot, defined as follows:

$$\Delta p = \frac{1}{\rho V_j^2 A} \int_A \{(p^e(x_1, x_3, t) - p^i(x_1, x_3, t))\} \mathrm{d}A,$$

$$Q = \frac{1}{V_j A} \int_A u_2^e(x_1, x_3, t) \mathrm{d}A,$$

where $p^e(x_1, x_3, t)$ and $p^i(x_1, x_3, t)$ denote the pressure at the slot exit and inlet, respectively, ρ is the density of the fluid and A is the cross-sectional area of the orifice. The plot indicates a sinusoidal variation in the flow rate, and this is consistent with the fact that we provide a sinsoidal volume flux at the bottom boundary of the cavity. The pressure variation also seems nearly sinusoidal and this is confirmed by examining the frequency spectra of the pressure drop variation which is plotted in figure 18(*b*). The spectra shows a dominant peak at the jet frequency. The next highest peak is at $3\,f_j$, but this is over two orders of magnitude lower than the peak at the fundamental frequency.

The linear acoustic impedence is a measure of the resistance experienced by the flow, and this quantity is a key component in low-dimensional actuator models such as those of Gallas *et al.* (2004*b*). The linear acoustic impedence Z for the current slot is defined as the ratio of the complex Fourier coefficient $\widehat{\Delta p}$ corresponding to the fundamental mode in Δp to the complex Fourier coefficient $\widehat{Q}$ corresponding to the dominant mode in Q, i.e.

$$Z = \frac{\widehat{\Delta p}}{\widehat{Q}} = \frac{|\widehat{\Delta p}| \exp(\mathrm{i}\theta_1)}{|\widehat{Q}| \exp(\mathrm{i}\theta_2)} = \frac{|\widehat{\Delta p}|}{|\widehat{Q}|} \exp(\mathrm{i}(\theta_1 - \theta_2)) = |Z| \exp(\mathrm{i}\psi),$$

where $\psi = \theta_1 - \theta_2$ is the phase lag, in radians, between Δp and Q. The linear acoustic impedance in the computations is determined to be $Z = |Z| \exp(\mathrm{i}\,\psi) = 0.621$

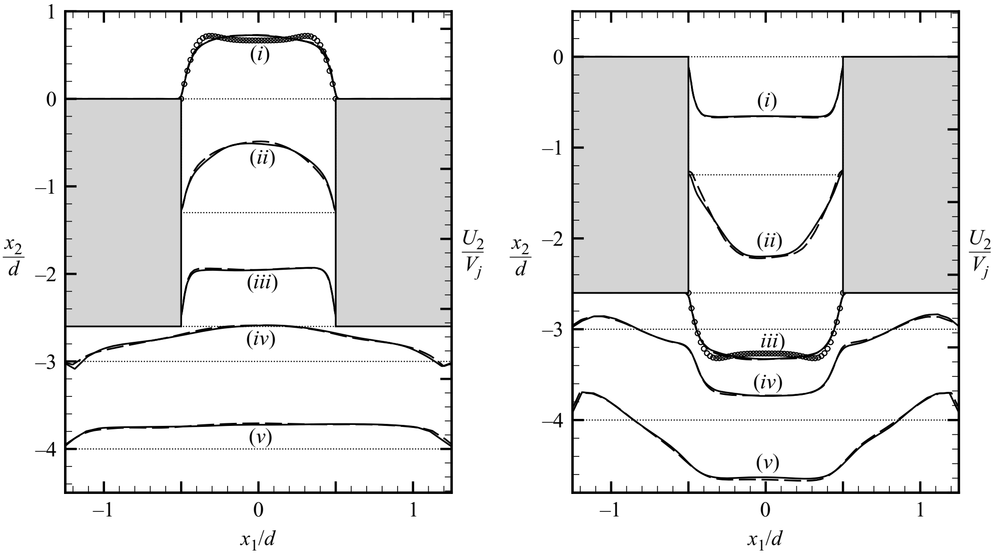

FIGURE 19. Profiles of phase-averaged streamwise velocity U_2/V_j in the slot and cavity at phase angles (*a*) $\phi = 92.6°$ and (*b*) $\phi = 272.6°$. The profile locations are (*i*) $x_2/d = 0$, (*ii*) -1.3, (*iii*) -2.6, (*iv*) -3.0 and (*v*) -4.0. - - -, Case 3; ———, Case 5; ○, fully developed oscillatory channel flow solution for $S = 17.0$. Note that the major tick mark spacing on the vertical axis U_2/V_j is $2V_j$.

$\exp(\mathrm{i}\,4.619)$. Note that a purely inviscid solution of fully developed oscillatory flow in the slot (Panton 1996) leads to an impedance which is given by $[2\pi\,St\,(h/d)]\exp(\mathrm{i}\,\frac{3\pi}{2}) = 0.65\exp(\mathrm{i}\,4.712)$ which matches reasonably well with the computed impedence. This implies that for this slot, the pressure drop is primarily determined by the unsteady inviscid volume flux and that entrance/exit and viscous effects play a minor nonlinear role in modifying the pressure drop. Thus, even though the instantaneous flow through the slot is different from a corresponding inviscid flow, the pressure–velocity relationship of the flow in the slot is similar to an inviscid flow. This is a further indication of the robustness of this flow, and its apparent lack of sensitivity to geometrical details of the jet cavity and slot.

Figure 19(*a*) shows the computed cross-stream distributions of the phase-averaged streamwise velocity U_2/V_j at $\phi = 92.6°$ at five different stations. A similar plot at $\phi = 272.6°$ (close to maximum ingestion phase) is shown in figure 19(*b*). Whereas the stations $x_2/d = 0.0, -1.3$ and -2.6 correspond to the slot exit, slot centre and slot inlet, respectively, the stations $x_2/d = -3$ and -4 correspond to locations inside the cavity. We observe that both during expulsion and ingestion there is significant variation in the velocity profiles across the length of the slot, reaffirming that the flow in the slot is highly non-developed.

In order to further explore this issue, it is useful to compare the profile in the slot with a profile corresponding to the fully developed laminar flow in a channel produced by a sinusoidal pressure gradient at the same Stokes number. The solution for this flow can be obtained analytically by integrating the Navier–Stokes equations (Loudon & Tordesillas 1998), and in figure 19 we have also shown this solution at the two different phases in the cycle superposed on the exit flow profile. A visual inspection shows that the profile at the midplane of the slot is significantly different from the fully developed profile. However, the profile at the top (bottom) of the

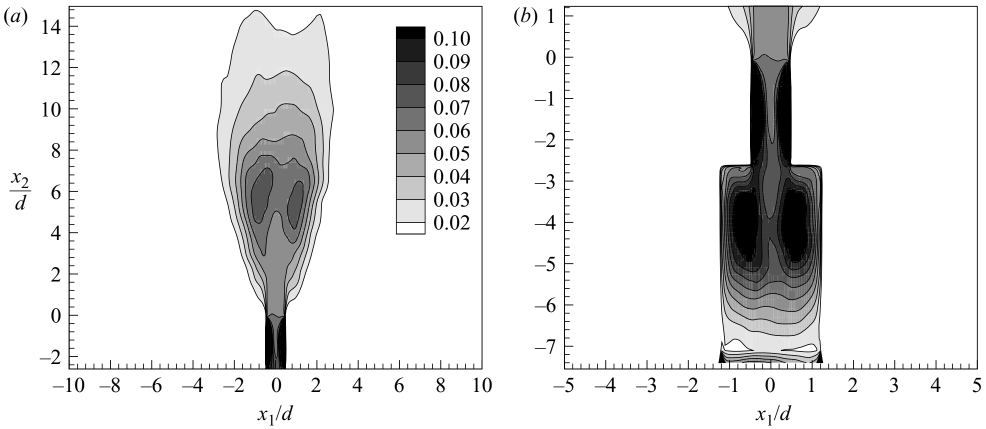

FIGURE 20. Contours of turbulent kinetic energy $\langle u_i'' u_i'' \rangle/(2V_j^2)$ obtained for Case 5: (*a*) external jet, and (*b*) slot and cavity region.

slot during expulsion (ingestion) matches the fully developed profile near the walls, but does not show the characteristic double-peaks (Lee & Goldstein 2002). The difference between the observed profiles and the fully developed profiles are due to both entrance/end-effects and to the presence of strong three-dimensional structures in the slot which would tend to diffuse and redistribute the momentum across the slot.

The flow at the bottom (top) of the slot during expulsion (ingestion) is nearly 'plug-like' and can essentially be modelled as a uniform flow. Finally, comparison of ingestion and expulsion phases shows that the velocity profiles at the centre of the slot during these two phases are noticeably different in shape. This difference is a manifestation of the inherent asymmetry between the external and internal flow fields. Thus, the flow in the slot during ingestion cannot simply be considered a mirror image of the flow during expulsion and this also has implications for the development of models and scaling laws for the slot flow. Inside the cavity, we observe mostly a unidirectional flow during expulsion, whereas large reverse flow regions are found to be present during ingestion.

3.7. *Turbulence characteristics*

Figure 20(*a*) shows a contour plot of the turbulent kinetic energy per unit mass which is defined as $\langle u_i'' u_i'' \rangle/2$ non-dimensionalized by V_j^2 for Case 5. Note that the u_i'' does not include the low-frequency coherent part of the velocity fluctuations and is therefore a true measure of the small-scale stochastic motions in the flow. The contour plot shows that in the external jet, the highest-intensity turbulence fluctuations occur at a distance of about $5.5d$ from the jet exit. Referring to figures 9 and 10, we find that this is the region where the vortices become highly three-dimensional and lose their coherence. Thus, it is not surprising that the highest turbulence intensity occurs in this region.

A contour plot of the turbulent kinetic energy inside the slot and the cavity is shown in figure 20(*b*) for Case 5. First, we find that the highest turbulence intensity is associated with the two boundary layers that form on the slot walls. These boundary layers are also found to separate and form *vena contractas* at the slot openings. Again referring to figure 10, we notice that both during the ingestion and expulsion parts of the cycles, three-dimensional vortical structures from the external and internal cavity

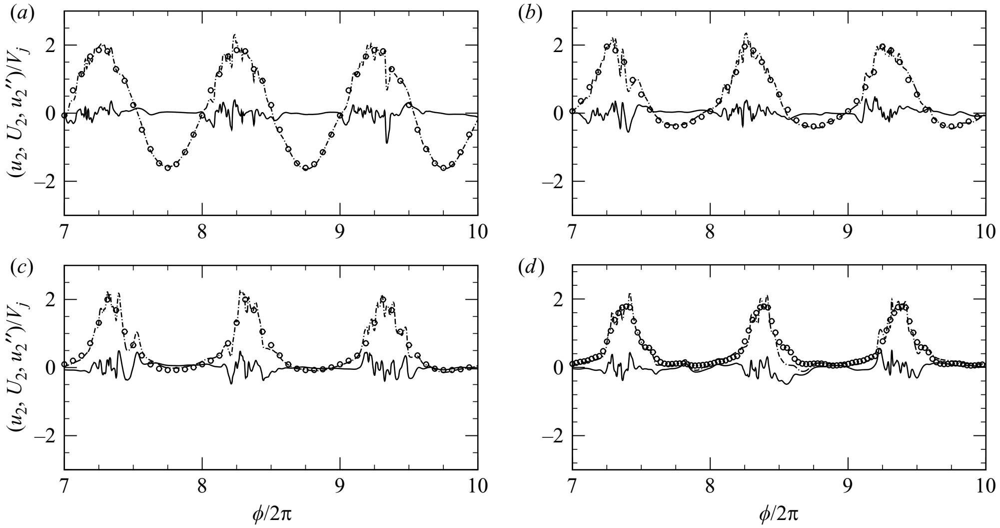

FIGURE 21. Temporal variations of instantaneous streamwise velocity u_2/V_j, phase-averaged streamwise velocity U_2/V_j and turbulent fluctuation u_2''/V_j outside the slot along the centreline $x_1/d = 0$ in the symmetry plane $x_3/d = 0$ for Case 5: (*a*) $x_2/d = 0$, (*b*) 1.0, (*c*) 1.93 and (*d*) 2.89. —·—, u_2/V_j; ——, u_2''/V_j; ○, U_2/V_j.

flow are ingested into the slot and these quickly destabilize the separated boundary layers. Within the cavity, local regions of high turbulence intensity are associated with the regions where the vortex pair, formed during the ingestion stroke, undergoes three-dimensional breakdown. The general behaviour is similar to that seen in the external flow, but the location of high intensity is much closer to the slot opening because of the confinement of the flow.

We now focus on the temporal variations and the frequency spectra of streamwise velocity fluctuations at several stations along the jet centreline for Case 5. At any given (x_1, x_2) location, the frequency spectrum is averaged along the homogeneous spanwise direction. Figures 21 and 22 show the temporal variations of the streamwise velocity (u_2/V_j), the phase averages of the streamwise velocity (U_2/V_j) and the corresponding velocity fluctuations (u_2''/V_j) at eight different streamwise locations along the jet centreline in the symmetry plane $(x_3 = 0)$. The instantaneous streamwise velocity is averaged in 24 phase bins, and the corresponding velocity fluctuations are obtained by subtracting the linearly interpolated phase averages from the instantaneous velocity.

The temporal variations in the near-field ($x_2/d \approx 0$ to 3) in figure 21 show that, as expected, the peak in the phase-averaged streamwise velocity occurs later in the cycle as we move further away from the jet slot. Also, the plots clearly show that irrespective of distance from the jet exit, stochastic turbulent fluctuations as indicated by u_2''/V_j occur almost exclusively during the expulsion phase (positive jet centreline exit velocity) in the cycle, and centre around the phase where the local phase-averaged velocity is at its maximum. During the ingestion part of the stroke, the flow accelerates towards the slot and this tends to stabilize the flow. Consequently, the fluctuation level during this phase of the cycle is very small.

The behaviour of the velocity fluctuation inside the slot and the cavity ($x_2/d < 0$), on the other hand, is quite different. Figure 22, which shows the velocity variations in these regions, clearly indicates that turbulent fluctuations occur primarily during the acceleration phase of the cycle, i.e. during the phase of the cycle when the

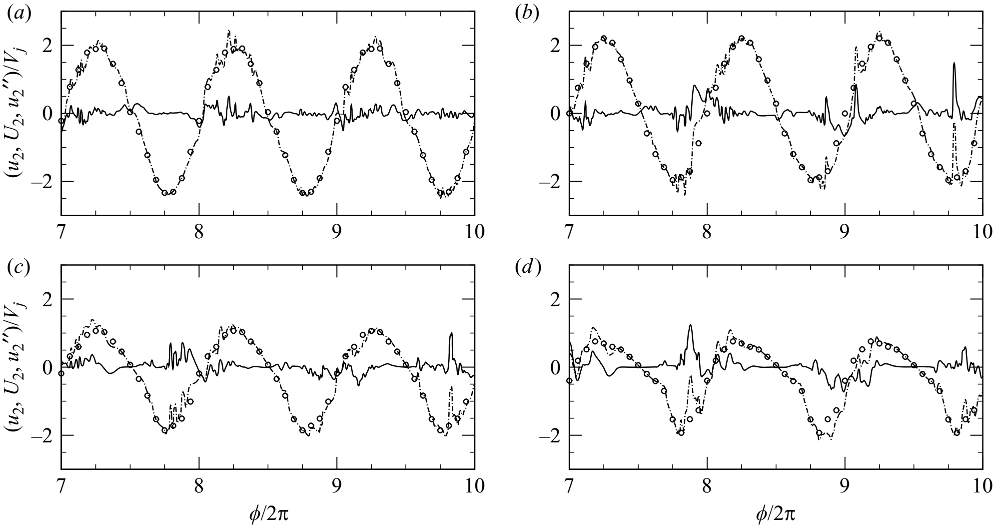

FIGURE 22. Temporal variation of instantaneous streamwise velocity u_2/V_j, phase-averaged streamwise velocity U_2/V_j and turbulent fluctuation u_2''/V_j inside the slot and cavity along the centreline $x_1/d = 0$ in the symmetry plane $x_3/d = 0$ for Case 5: (*a*) $x_2/d = -1.0$, (*b*) −2.0, (*c*) −3.0 and (*d*) −4.0. —·—, u_2/V_j; ——, u_2''/V_j; ○, U_2/V_j.

bulk velocity increases from its minimum value to its maximum. This is in direct contrast to what has been observed for oscillatory (zero mean) or pulsatile (non-zero mean) pipe/channel flows where turbulent fluctuations are found primarily during the deceleration phase (Winter & Nerem 1984; Mittal *et al.* 2003). The precise mechanism responsible for this unexpected behaviour is not currently understood, but is probably because, unlike pulsatile channel flow where the turbulence is triggered by a instability of the bulk flow, the turbulence in the current flow is primarily associated with detached shear layers both inside and outside the cavity as well as the slot walls. Thus, we suspect that the turbulent fluctuations that appear in the slot are, in fact, initiated in the cavity below, and convected into the slot during expulsion. The current flow is also highly non-homogeneous in the streamwise direction in the vicinity of the slot, and this is not the case for pulsatile channel flow which is essentially homogeneous in the streamwise direction. Thus, transition to turbulence in the current flow may be triggered by completely different mechanisms.

Examination of the frequency spectra corresponding to these velocity fluctuations can shed more light on the dynamics of the flow and transition phenomena. The frequency spectra corresponding to the velocity fluctuations u_2''/V_j in figures 21 and 22 are shown in figure 23. The temporal variations shown in figures 21 and 22 correspond to one selected spanwise station, whereas the frequency spectra are obtained by averaging the individual spectral densities at a particular (x_1, x_2) location across the span. The angular frequency ($\omega_k = 2\pi f k$, where f is the frequency) in these plots is non-dimensionalized by V_j/d and the spectral density $E_{u_2u_2}(\omega_\kappa)$ is obtained by normalizing the power by $\Delta\omega$. Therefore, the spectrum $E_{u_2u_2}(\omega_k)$ represents the contribution to $\langle u_2''u_2''\rangle$ from the frequency band ω_k to $\omega_k + \Delta\omega$. Also included in these plots are the lines corresponding to $\kappa^{-5/3}$ and κ^{-7} variations. Whereas the $\kappa^{-5/3}$ variation is associated with the inertial subrange (Tennekes & Lumley 1972), the κ^{-7} variation characterizes the dissipation range (Hinze 1975) where most of the turbulent kinetic energy is dissipated by the action of the viscosity.

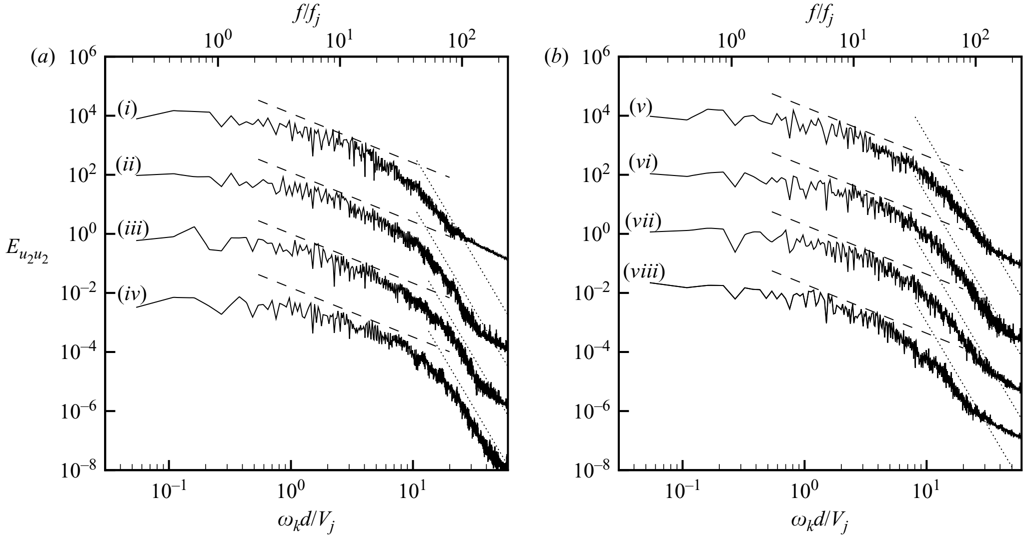

FIGURE 23. Frequency spectra corresponding to temporal variation of u_2'' along the centreline $x_1/d = 0$ in the symmetry plane $x_3/d = 0$ for Case 5: (*i*) $x_2/d = 2.89$, (*ii*) 1.93, (*iii*) 1.0, (*iv*) 0, (*v*) −1.0, (*vi*) −2.0, (*vii*) −3.0 and (*viii*) −4.0. Note that the spectra at $x_2/d = 1.0, 1.93$ and 2.89 are offset in the vertical direction from the spectrum at $x_2/d = 0$ by two, four and six decades, respectively. The same applies to the spectra at $x_2/d = -2.0, -3.0$ and −4.0 with reference to the spectrum at $x_2/d = -1.0$. ———, $E_{u_2u_2}$; - - -, $\kappa^{-5/3}$; ···, κ^{-7}.

A noticeable inertial subrange and dissipation range in the spectra at $x_2/d \approx 1$, 2 and 3 in figure 23(*a*) indicates a well-developed turbulent flow at these stations. Since the Reynolds number is not very large, the dissipating eddies are only slightly smaller than the energy-containing eddies and so the inertial subrange is quite narrow at $x_2/d \approx 0$ and broadens as we move away from the jet exit plane. In the cavity at $x_2/d \approx -4$, the spectrum shown in figure 23(*b*) depicts a relatively short inertial subrange and a distinct dissipation range associated with the turbulent flow at this station. However, as we move up towards the slot, the inertial range narrows further and the dissipation range departs from the −7 slope. Thus, even though the turbulent kinetic energy in the slot is high, the spectra indicate that turbulence in this region is not well developed. On the other hand, as we move away from the slot ends in either direction, the flow shows more evidence of being a well-developed turbulent flow. The spectra also provide indirect evaluation of the spatial and temporal resolution in the current simulations. The ‘tail’ in each spectra, i.e. the point in the spectra at the higher frequencies where there is a noticeable deviation from the κ^{-7} line, indicates the extent of the frequencies and scales that are adequately resolved in the current simulations. Thus, the spectra clearly show that the simulations resolve scales deep into the dissipation range, thereby further confirming the accuracy of the current computations.

4. Conclusions

The evolution of a synthetic jets exhausting into a quiescent external flow and transitioning to turbulence has been studied using three-dimensional direct numerical simulations. The simulations were nominally designed to match the experiments of Yao *et al.* (2004*b*). In particular, care was taken to match the jet Reynolds number and

Stokes number which also ensures a matching of the jet Strouhal number. However, guided by physical reasoning, we chose an actuator geometry that was significantly different and simpler than the one in the experiment. Despite the differences between the experimental and computational flow configurations, we found a reasonably good match between the two in the outer flow, at least up to about four slot widths downstream of the jet exit after which edge-effects become important.

Flow visualizations indicate that the near-field is dominated by counter-rotating vortex pairs that convect downstream by self-induction. The simulations also show the presence of mostly streamwise oriented rib-like secondary vortical structures surrounding the cores of the primary vortex pair. These secondary structures undergo rapid amplification owing to three-dimensional vortex stretching, and cause transition of the primary vortex pair into a well-developed turbulent jet within a short distance from the orifice. This is verified by examining the velocity spectra in these regions. During the ingestion cycle, counter-rotating vortices form inside the cavity, and the flow in this region also transitions to a well-developed turbulent flow. Within the slot, the turbulence intensity is high, but the turbulence is not in equilibrium.

In addition to shedding light on the flow physics of this flow, a key contribution of the current work is the strong reaffirmation of the notion previously put forth by Smith & Swift (2001), Utturkar & Mittal (2002), Utturkar *et al.* (2003) and Holman *et al.* (2005) that the jet Strouhal number is the key parameter in these flows. In particular, using a sequence of simulations, we have demonstrated that the vortex trajectory and celerity are primarily determined by this parameter and successful comparison with experiments depends critically on matching this parameter. Our simulations also show that at least in the incompressible regime, the details of the cavity do not significantly affect the external jet flow and that even a rudimentary representation of the jet slot is sufficient to enable a good prediction of the jet features. This has important implications for computational modelling of synthetic jets in flow control and other applications since it implies that simple geometrical models of the jet that do not significantly increase the grid requirements could be employed. Furthermore, in addition to comparing the external flow with available experimental data, we have also provided data on the cavity and slot flow, and we expect that this data will find use in the development and testing of low-dimensional actuator models and in future numerical validation efforts.

This work was supported by National Aeronautics and Space Administration (Grant NAG-1-01024) and US Air Force Office of Scientific Research (Grant F49620-03-1-0146 to RM and FA9550-05-1-0093 to LNC).

REFERENCES

Amitay, M., Honohan, A., Trautman, M. & Glezer, A. 1997 Modification of the aerodynamic characteristics of bluff bodies using fluidic actuators. *AIAA Paper* 97-2004.

Amitay, M., Kibens, V., Parekh, D. & Glezer, A. 1999 The dynamics of flow reattachment over a thick airfoil controlled by synthetic jet actuators. *AIAA Paper* 99-1001.

Andres, J. M. & Ingard, U. 1953 Acoustic streaming at high Reynolds numbers. *J. Acoust. Soc. Am.* **25**, 928–932.

Crook, A., Sadri, A. M. & Wood, N. J. 1999 The development and implementation of synthetic jets for the control of separated flow. *AIAA Paper* 99-3176.

Dong, H., Mittal, R. & Najjar, F. M. 2006 Wake topology and hydrodynamic performance of low-aspect-ratio flapping foils. *J. Fluid Mech.* **566**, 309–343.

Gallas, Q. 2005 On the modeling and design of zero-net mass flux actuators. PhD thesis, University of Florida.

Gallas, Q., Holman, R., Nishida, T., Carroll, B., Sheplak, M. & Cattafesta, L. 2003*a* Lumped element modeling of piezoelectric-driven synthetic jet actuators. *AIAA J.* **41**, 240–247.

Gallas, Q., Wang, G., Papila, M., Sheplak, M. & Cattafesta, L. 2003*b* Optimization of synthetic jet actuators. *AIAA Paper* 2003-0635.

Gallas, Q., Holman, R., Raju, R., Mittal, R., Sheplak, M. & Cattafesta, L. 2004*a* Low dimensional modeling of zero-net mass-flux actuators. *AIAA Paper* 2004-2413.

Gallas, Q., Mittal, R., Sheplak, M. & Cattafesta, L. 2004*b* Case 1: Lumped element modeling of a zero-net mass flux actuator issuing into a quiescent medium. In *Proc. NASA LaRC Workshop on CFD Validation of Synthetic Jets and Turbulent Separation Control, Williamsburg, Virginia, March 29–31*.

Glezer, A. & Amitay, M. 2002 Synthetic jets. *Annu. Rev. Fluid Mech.* **34**, 503–532.

Hinze, J. O. 1975 *Turbulence*, 2nd edn. McGraw-Hill.

Holman, R. 2006 An experimental investigation of flows from zero-net mass-flux actuators. PhD thesis, University of Florida.

Holman, R., Utturkar, Y., Mittal, R., Smith, B. L. & Cattafesta, L. 2005 Formation criterion for synthetic jets. *AIAA J.* **43**, 2110–2116.

Ingard, U. & Labate, S. 1950 Acoustic circulation effects and the nonlinear impedance of orifices. *J. Acoust. Soc. Am.* **22**, 211–218.

James, R. D., Jacobs, J. W. & Glezer, A. 1996 A round turbulent jet produced by an oscillating diaphragm. *Phys. Fluids* **8**, 2484–2495.

Kaltenbach, H.-J., Fatica, M., Mittal, R., Lund, T. S. & Moin, P. 1999 Study of flow in a planar asymmetric diffuser using large-eddy simulation. *J. Fluid Mech.* **390**, 151–186.

Kral, L. D., Donovan, J. F., Cain, A. B. & Cary, A. W. 1997 Numerical simulation of synthetic jet actuators. *AIAA Paper* 97-1824.

Lebedeva, I. V. 1980 Experimental study of acoustic streaming in the vicinity of orifices. *Sov. Phys. Acoust.* **26**, 331–333.

Lee, C. Y. & Goldstein, D. B. 2001 DNS of microjets for turbulent boundary layer control. *AIAA Paper* 2001-1013.

Lee, C. Y. & Goldstein, D. B. 2002 Two-dimensional synthetic jet simulation. *AIAA J.* **40**, 510–516.

Leonard, B. P. 1979 A stable and accurate convection modeling procedure based on quadratic upstream interpolation. *Comput. Methods Appl. Mech. Engng* **19**, 59–98.

Loudon, C. & Tordesillas, A. 1998 The use of the dimensionless Womersley number to characterize the unsteady nature of internal flow. *J. Theor. Biol.* **191**, 63–78.

Mallinson, S. G., Hong, G. & Reizes, A. J. 1999 Some characteristics of synthetic jets. *AIAA Paper* 99-3651.

Mednikov, E. P. & Novitskii, B. G. 1975 Experimental study of intense acoustic streaming. *Sov. Phys. Acoust* **21**, 152–154.

Meissner, A. 1926 Uber piezo-elektrische kristalle bei hoch-frequenz. *Z. Tekh. Fiz* **7**, 585.

Mittal, R. 2000 Response of the sphere wake to freestream fluctuations. *Theoret. Comput. Fluid Dyn.* **13**, 397–419.

Mittal, R. & Balachandar, S. 1997 On the inclusion of three-dimensional effects in simulations of two-dimensional bluff-body wake flows. In *Proc. 1997 ASME Fluids Engng. Div. Summer Meeting, Vancouver, Canada*.

Mittal, R., Rampunggoon, R. & Udaykumar, H. S. 2001 Interaction of a synthetic jet with a flat plate boundary layer. *AIAA Paper* 2001-2773.

Mittal, R., Simmons, S. P. & Najjar, F. 2003 Numerical study of pulsatile flow in a constricted channel. *J. Fluid Mech.* **485**, 337–378.

Najjar, F. M. & Mittal, R. 2003 Simulations of complex flows and fluid-structue interaction problems on fixed Cartesian grids. In *Proc. FEDSM'03, 4th ASME–JSME Joint Fluids Engng Conf., Honolulu, Hawaii*, pp. 184–196.

Panton, R. L. 1996 *Incompressible Flow*, 2nd edn. John Wiley.

Raju, R., Mittal, R., Gallas, Q. & Cattafesta, L. 2005 Scaling of vorticity flux and entrance length effects in zero-net mass-flux devices. *AIAA Paper* 2005-4751.

Rathnasingham, R. & Breuer, K. S. 1997 System identification and control of a turbulent boundary layer. *Phys. Fluids* A **9**, 1867–1869.

RATHNASINGHAM, R. & BREUER, K. S. 2003 Active control of turbulent boundary layers. *J. Fluid Mech.* **495**, 209–233.

RAVI, B. R., MITTAL, R. & NAJJAR, F. M. 2004 Study of three-dimensional synthetic jet flowfields using direct numerical simulations. *AIAA Paper* 2004-0091.

REYNOLDS, W. C. & HUSSAIN, A. K. M. F. 1972 The mechanics of an organized wave in turbulent shear flow. Part 3. theoretical models and comparisons with experiments. *J. Fluid Mech.* **54**, 263–288.

RIZZETTA, D. P., VISBAL, M. R. & STANEK, M. J. 1999 Numerical investigation of synthetic-jet flowfields. *AIAA J.* **37**, 919–927.

RUMSEY, C. L., GATSKI, T. B., SELLERS, W. L., VATSA, V. N. & VIKEN, S. A. 2004 Summary of the 2004 CFD validation workshop on synthetic jets and turbulent separation control. *AIAA Paper* 2004-2217.

SHEEN, S. H., LAWRENCE, W. P. & RAPTIS, A. C. 1989 Cavitation-controlled ultrasonic agitator. In *Proc. IEEE Ultrasonics Symp.* vol. 1, pp. 653–656.

SMITH, B. & SWIFT, G. 2001 Synthetic jets at large Reynolds number and comparison to continous jets. *AIAA Paper* 2001-3030.

SMITH, B. L. & GLEZER, A. 1998 The formation and evolution of synthetic jets. *Phys. Fluids* **10**, 2281–2297.

SMITH, B. L. & GLEZER, A. 2002 Jet vectoring using synthetic jets. *J. Fluid Mech.* **458**, 1–34.

SMITH, D. & GLEZER, A. 1997 Vectoring and small-scale motions effected in free shear flows using synthetic jet actuators. *AIAA Paper* 97-0213.

SMITH, D., AMITAY, M., KIBENS, V., PAREKH, D. & GLEZER, A. 1998 Modification of lifting body aerodynamics using synthetic jet actuators. *AIAA Paper* 98-0209.

SORIA, J. & CANTWELL, B. J. 1993 Identification and classification of topological structures in free shear flows. In *Eddy Structure Identification in Free Turbulent Shear Flows* (ed. J. P. Bonnet & M. N. Glauser), pp. 379–390. Kluwer.

TENNEKES, H. & LUMLEY, J. L. 1972 *A First Course in Turbulence*, 1st edn. The MIT Press.

UDAYKUMAR, H. S., MITTAL, R., RAMPUNGGOON, P. & KHANNA, A. 2001 A sharp interface Cartesian grid method for simulating flows with complex moving boundaries. *J. Comput. Phys.* **174**, 345–380.

UTTURKAR, Y. & MITTAL, R. 2002 Senitivity of synthetic jets to the design of the jet cavity. *AIAA Paper* 2002-0124.

UTTURKAR, Y., HOLMAN, R., MITTAL, R., CARROLL, B., SHEPLAK, M. & CATTAFESTA, L. 2003 A jet formation criterion for synthetic jet actuators. *AIAA Paper* 2003-0636.

WHITE, F. M. 1991 *Viscous Flow*, 2nd edn. McGraw-Hill.

WINTER, D. C. & NEREM, R. M. 1984 Turbulence in pulsatile flows. *Ann. Biomed. Engng* **12**, 357–369.

WYGNANSKI, I. 1997 Boundary layer and flow control by periodic addition of momentum. *AIAA Paper* 97-2117.

YAO, C. S., CHEN, F. J., NEUHART, D. & HARRIS, J. 2004*a* Synthetic jet flow database for CFD validation. *AIAA Paper* 2004-2218.

YAO, C. S., CHEN, F. J., NEUHART, D. & HARRIS, J. 2004*b* Synthetic jets in quiescent air. In *Proc. NASA LaRC Workshop on CFD Validation of Synthetic Jets and Turbulent Separation Control, Williamsburg, Virginia, March 29–31*.

YE, T., MITTAL, R., UDAYKUMAR, H. S. & SHYY, W. 1999 An accurate Cartesian grid method for viscous incompressible flows with complex immersed boundaries. *J. Comput. Phys.* **156**, 209–240.